This manuscript has been submitted for publication in *Science of The Total Environment* on 24^{th} June 2022. Please note that the manuscript has not yet undergone peer-review. Hence, the manuscript has yet to be formally accepted for publication. Subsequent versions of this manuscript may have slightly different content. If accepted, the final version of this manuscript will be available via the 'Peer-reviewed Publication DOI' link on the right-hand side of this webpage. Please feel free to contact any of the authors; we welcome feedback.

Barren ground depressions, natural H_2 and orogenic gold deposits: spatial link and geochemical model

Benjamin Malvoisin[a,*], Fabrice Brunet[a]

[a]1 Univ. Grenoble Alpes, Univ. Savoie Mont Blanc, CNRS, IRD, Univ. Gustave Eiffel, ISTerre, 38000 Grenoble, France

Abstract

A review of the localities in continental rocks where H_2-rich gases have been reported, showed that they are mainly located near gold deposits. Two types of geomorphological features known as markers of gas venting in sedimentary basins were also systematically observed near orogenic gold deposits on satellite images. They consist in both barren ground depressions and high densities of small (< 20 m in diameter) circular- and comet-shaped white spots in 32 and 7 localities, respectively. Point pattern analysis revealed that the white spots are self-organized, and similar to previously described vegetation patterns including termite mounds and fairy circles. We proposed a geochemical model to account for this relationship between orogenic gold deposits, H_2 emanations and geomorphological features. Fe-carbonates are ubiquitous mineral products associated with gold mineralization. They can further dissolve in the presence of aqueous fluid due to their high reactivity below 200°C to produce magnetite and up to $\sim$ 1 mole of H_2 per kg of rock along with $\sim$ 3 mol/kg CO_2. This process induces a solid volume decrease of 50 %. Therefore, we propose that Fe-carbonate dissolution is (1) the primary source of H_2 in orogenic gold deposit areas, and (2) involved in the formation of the geomorphological structures reported here, providing a new framework to understand their seemingly complex formation. Ground depressions and white spots are possible tools for gold explorations. Actually, we identified four new areas where we suspect possible orogenic gold deposits. The association between H_2-rich gas and ground depressions was also made near other formations containing Fe-carbonates such as iron formations and carbonatites. This suggests that H_2 production through Fe-carbonate dissolution is not restricted to gold deposits. The global H_2 production in crustal rocks associated with Fe-carbonate alteration is estimated to 3.10^5 mol/yr.

Keywords: natural hydrogen, abiotic methane, siderite, ankerite, thermodynamic modelling, low-temperature alteration, iron formation, carbonatite, fairy circles, gas venting, termite mounds, mima mounds, vegetation patterns

Graphical abstract

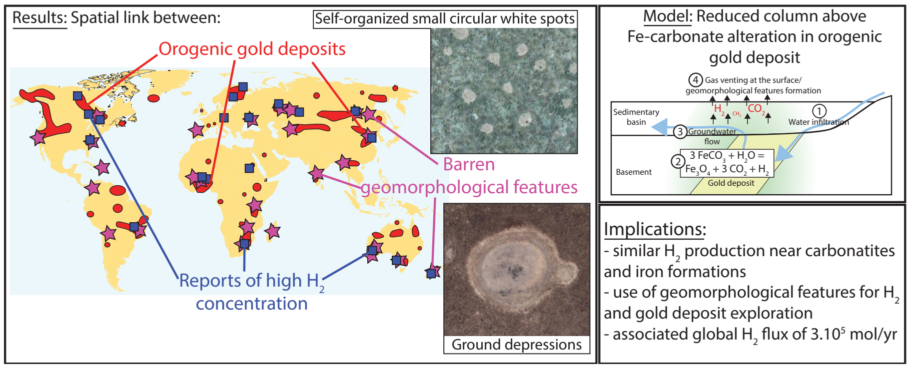

1. Introduction

To limit greenhouse gases emissions, hydrogen (H_2) is considered as an alternative to fossil fuels in particular in the transportation sector (Acar and Dincer, 2020) where H_2 can be used either as a fuel in internal combustion engines or as a reagent in H_2 fuel cells for electric vehicles. However, most of the hydrogen currently produced at the industrial scale involves fossil fuel reforming, a process that releases CO_2 (Dincer and Acar, 2014). The challenge in making hydrogen a green energy vector thus consists in the development of low-carbon H_2 production processes (e.g., from renewable energies, Chi and Yu (2018); biomass, Lu et al. (2012); or waste recycling, Brunet (2019)). Another option would be for H_2 to be available as a natural gas in significant quantities to meet the needs of the energy transition. In fact, there is now compelling evidence of anomalously high H_2 concentrations in natural gas sampled in a variety of geological settings, both onshore and offshore (Zgonnik, 2020), i.e. with concentrations far above the 550 ppb atmospheric level (Novelli, 1999). The idea that natural H_2 could accumulate underground to form a natural resource is gradually emerging even though natural H_2 exploration is still in its infancy and the origin of natural H_2 is still debated.

It is now well-established that serpentinization reactions which result from the chemical interaction between upper-mantle rocks (ultramafic rocks) and water at temperatures below 350°C (Cannat et al., 2010; Klein et al., 2020) are a major source of natural and abiotic H_2. Hydrogen is mainly produced together with magnetite (Fe_3O_4) through the oxidation of the ferrous iron contained in olivine, $(Mg,Fe)_2SiO_4$, the main mineral component of mantle rocks (Malvoisin et al., 2012; McCollom et al., 2016). H_2 gas produced by serpentinization has

*Corresponding author: benjamin.malvoisin@univ-grenoble-alpes.fr

been reported at mid-ocean ridges (Charlou et al., 2002), in ophiolites (Neal and Stanger, 1983; Abrajano et al., 1990; Deville and Prinzhofer, 2016; Etiope et al., 2017) and in orogenic belts (Lefeuvre et al., 2021). Fischer-Tropsch type reactions are believed to occur in ultramafic-hosted hydrothermal systems leading to light hydrocarbons (including CH_4) production (Berndt et al., 1996; Charlou et al., 2002; Proskurowski et al., 2008; Etiope and Sherwood Lollar, 2013; Etiope, 2017). These latter reactions require metal-catalysts to proceed at temperatures below 400°C (McCollom, 2013).

Besides the rather well-constrained abiotic H_2 production described above in ultramafic-hosted systems, other still enigmatic occurrences of natural hydrogen have attracted significant attention in the past years. For example, H_2 and light hydrocarbons occur as free and dissolved gas in Precambrian cratons (Sherwood Lollar et al., 2007, 2014). Carbon isotopic study revealed that CH_4 sampled in the Canadian shield and the Witwatersrand Basin (South Africa) can also be associated with abiogenic polymerization (Sherwood Lollar et al., 2008). Hydrogen has been sampled underground (in mines and in exploration boreholes) but also in soils of barren ground depressions found in sedimentary basins overlying Precambrian rocks in Mali (Prinzhofer et al., 2018), Brazil (Prinzhofer et al., 2019) and Australia (Frery et al., 2021; Mainson et al., 2022). Interestingly, all these localities where natural H_2 has been reported are also known as gold provinces. In addition, Zgonnik et al. (2015) measured several hundreds of ppm of H_2 in ground depressions at a fourth locality in the USA in Phanerozoic rocks bordering gold deposits. Ground depressions can be easily recognized on satellite images, and have been used for H_2 exploration in South Africa (Moretti et al., 2021; Geymond et al., 2022), which is a main gold producer. This geographic correlation may reveal a genetic link between ground depressions, H_2 emissions and gold deposits. It may also be fortuitous since several processes such as karst formation can lead to sinkhole formation with no measurable gas venting (Halas et al., 2021). Therefore, we have investigated here the possible spatial link (1) between gold deposits and H_2 emissions through a literature review, and (2) between gold deposits and geomorphological features through a systematic screening of satellite images in sedimentary basins overlying gold deposits worldwide.

Ground depressions containing H_2 have sometimes been named "fairy circles" by previous authors (Prinzhofer et al., 2019; Myagkiy et al., 2020b; Moretti et al., 2021; Frery et al., 2021). The genuine fairy circles found in Namibia, Angola and Australia are characterized by an occurrence in semi-arid regions, an absence of vegetation in their center, a circular shape, a small size (< 20 m in diameter), and an organization in spatially periodic patterns (Meyer et al., 2021; Getzin et al., 2021b). Based on these properties, Getzin et al. (2021b) recently pointed out that the name "fairy circles" should not be used for previously described ground depressions emitting H_2 due to their large size (up to several hundreds of meters) and to their disordered spatial distribution. Nevertheless, the morphology and the barren soil in the center of both ground depressions and fairy circles suggest that they could form by the same process. The formation of fairy circles sensu stricto is generally attributed to ecological processes including termite activity and self-organization due to plant competition in a water-limited ecosystem (Meyer et al., 2021). Microseepage of gas (carbon monoxide) and hydrocarbons has also been measured in fairy circles, suggesting a geochemical origin (Naudé et al., 2011). However, the reaction involved in gas production in the underlying rocks is still unknown, preventing a better understanding of fairy circle formation. Fairy circles are part of a wider group of regular self-organized vegetation patterns including termite mounds with barren soil in their center (Tarnita et al., 2017). Such patterns appear as high densities of small white spots on satellite images, and we included them in our screening of geomorphological features to show that fairy circles and termite mounds are also common near gold deposits.

The potential link between H_2-emitting structures and orogenic gold deposits can shed light on the H_2 origin itself. Indeed, the source of natural H_2 in Precambrian rocks is poorly constrained and generally attributed to Fe^{2+}-oxidation of silicates (e.g. serpentinization) in the adjacent mafic and ultramafic rocks (Sherwood Lollar et al., 2014; Boreham et al., 2021). However, other abiotic H_2 sources can also be invoked such as the interaction between water and Fe^{2+}-minerals that do not originate from ultramafic rocks (e.g., siderite, McCollom (2003); Milesi et al. (2015); biotite, Murray et al. (2020); arfvedsonite, Truche et al. (2021)), sulfide oxidation (Bach and Edwards, 2003), radiolysis of H_2O associated with the decay of Th, U and K (Ershov, 2020), the reaction between fresh silicate surfaces produced by crushing (faulting) and water (Kita et al., 1982) among others. The biological activity in soils has also been recognized as a source of H_2 gas, in particular, by N_2-fixing and fermenting bacteria (Conrad, 1996). However, the net effect of biological activity in soils with respect to H_2 is thought to be its consumption (Conrad and Seiler, 1980; Novelli, 1999; Myagkiy et al., 2020a). Subsurface microbial hydrogen cycling and hydrogen turnover rates in natural environments remain however poorly understood (Gregory et al., 2019).

2. Natural hydrogen occurrence in orogenic gold deposits: a literature review

We review below literature reports on the occurrence of H_2 and/or hydrocarbons in gases, groundwater and fluid inclusions in the vicinity of gold deposits. CH_4-bearing inclusions are ubiquitous in gold deposits and we therefore focus in the following on the report of H_2-bearing inclusions. Ground depressions associated with H_2 emanations are discussed in the next section. Figure 1 provides a map with the location of natural H_2 gas occurrence in gold provinces.

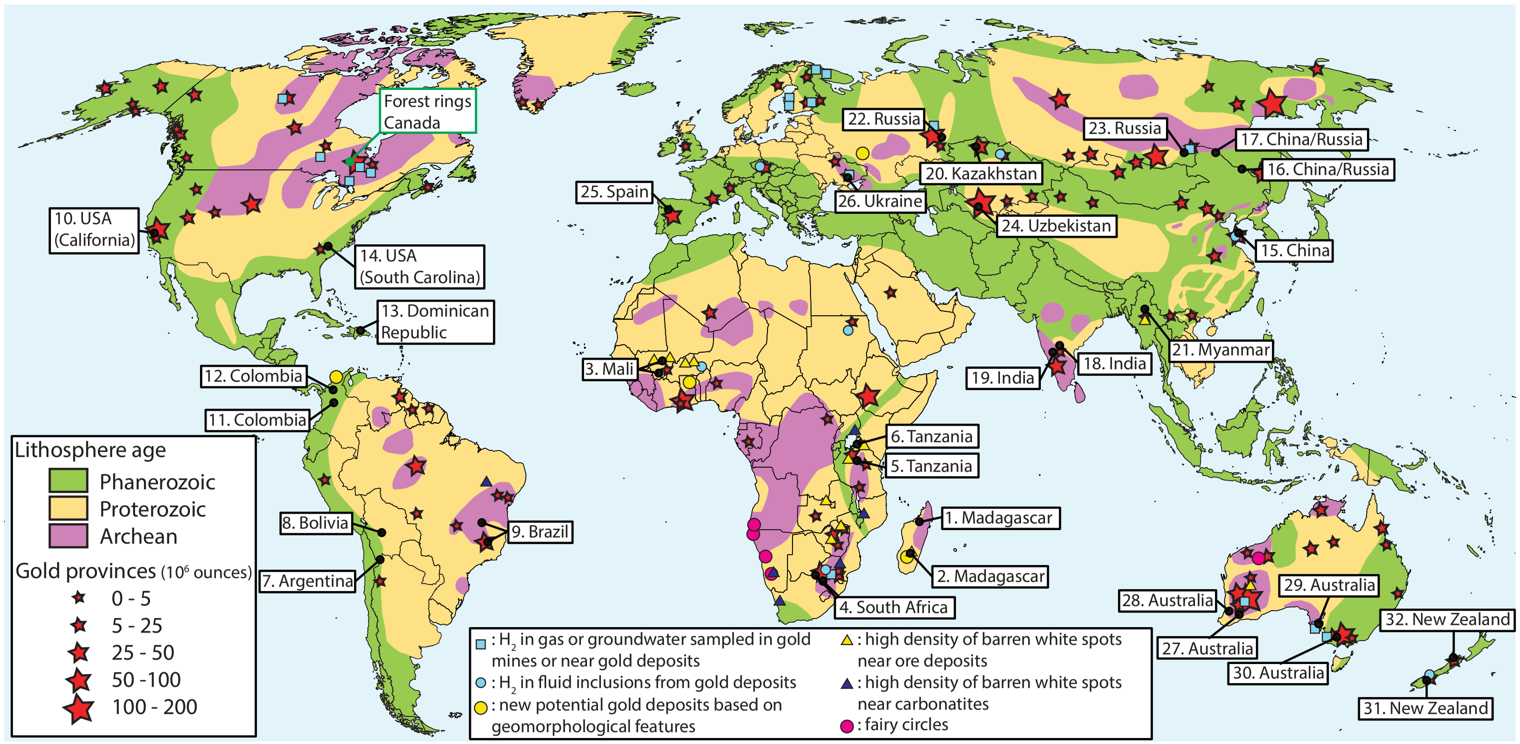

Figure 1: World map displaying the link between gold deposits and occurrence of natural H_2. The global distribution of gold deposits (after Goldfarb et al. (2001)) is superimposed on the lithosphere age (after Artemieva (2006)). Measurements of anomalously high natural H_2 concentrations in gas, groundwater and fluid inclusions in gold mineralizations are indicated with light blue symbols. The gold deposits studied here with nearby ground depressions (black dots) are numbered with a label indicating the country of origin. The location of circular depressions with low tree density (forest rings; Hamilton and Hattori (2008)) is indicated with a green dot. Based on the presence of typical geomorphological features, new potential orogenic gold deposits are marked with yellow dots. The orange and yellow triangles refer to locations where small ($<$ 20 m wide) barren white spots are observed near gold deposits and carbonatites, respectively. The pink dots indicate known location of fairy circles (Getzin et al., 2016; Meyer et al., 2021).

Reports of H_2 concentrations in gases above several hundreds of ppm are common in Precambrian rocks. In Canada, Sherwood Lollar et al. (1993a,b, 2006, 2007, 2014) measured H_2 concentrations up to 58 vol. % and CH_4 concentrations up to 74 vol. % in gold mines (Campbell, Dickenson, Kidd Creek, Val dOr, Con, Giant and Copper Cliff South mines). The mines are situated in the Archean Abitibi, Red Lake and Yellowknife Greenstone belts. Detailed mapping of the mineralogical assemblages distribution in the corresponding mines revealed the systematic presence of dense ankerite vein networks (Boyle, 1955; Dubé et al., 2003; Stromberg et al., 2018). Stromberg et al. (2018) estimated that ankerite represents 20 % of the deposit in Dome Mine (Timmins gold camp). Fe-rich carbonate is thought to form during ultramafic and felsic host rock carbonation associated with gold deposition. The only reported occurrence of H_2 outside gold mine provinces in Canada deals with a nickel mine (Thompson mine) where the maximum reported H_2 concentration is of 2.75 vol. % (Sherwood Lollar et al., 2014). In Finland, Sherwood Lollar et al. (1993a,b) and Pedersen (2000) sampled H_2 and hydrocarbons in gas and groundwater in eight localities in Precambrian rocks. Among them, six are located in gold belts and one near a volcanogenic massive sulfide deposit (Eilu, 2015). Enonkovki and Ylistaro localities are in the Southern Sato and Southern Ostrobothnia orogenic gold belts. Olkiluoto, Pori and Vammala sites occur in the Pirkanmaa gold belt, at less than 60 km from the Jokisivu gold mine. Flammable gases such as H_2 and CH_4 are widespread in South Africa gold mines where they can lead to gas accidents (Cook et al., 1999). Ward et al. (2004) and Sherwood Lollar et al. (2006, 2014) analyzed gas compositions in 5 mines of the Witwatersrand basin, one of the largest goldfield on Earth (Figure 1). They detected H_2 at concentration up to 10.3 vol. % in association with CH_4 at concentration up to 76 vol. %. Lin et al. (2005) also found dissolved H_2 in fracture water collected in the same mines of the Witwatersrand basin. Fluid inclusions in quartz $\pm$ carbonates veins also contain H_2 and CH_4 (Drennan et al., 1999). The origin of gold mineralization in this Archean intracratonic basin is controversial (Goldfarb et al., 2001). On the contrary to other orogenic gold deposit worldwide, quartz + carbonate veins are not ubiquitous in the Witwatersrand basin even though they can occur (Drennan et al., 1999). Fe-carbonates rather occur in association with iron formations and shales (Smith et al., 2013; Nwaila et al., 2021). In Australia, natural hydrogen was analyzed in the gas collected in a borehole drilled in the Yorke Peninsula (Ward, 1933; Woolnough, 1934). The Hillside gold deposit occurs on the Yorke Peninsula with carbonate-bearing assemblages formed during Precambrian (Cerlienco, 2009). Boreham et al. (2021) recently measured H_2 concentrations up to 76.9 mol. % in gas sampled in the Neoarchean Frog's Leg gold camp (Ylgarn craton; Western Australia). The gas also contains hydrocarbons with isotopic signatures suggesting formation through Fischer-Tropsch type reactions during H_2 interaction with CO_2. Fe-carbonate (ankerite) is ubiquitous in the hydrothermal alteration assemblages found in the Ylgarn craton (Mueller and Groves, 1991; Bateman and Hagemann, 2004). Zgonnik (2020) reported the presence of H_2 in some iron ore mines exploiting banded iron formation in the Kryvyi Rih region (Ukraine). Berezovsky et al. (2021) recently described gold mineralization together with hydrothermal carbonates at the same locality. Gold mineralization in banded iron formations were also described in the Olenegorsk belt of the Kola Province Kalinin et al. (2019). H_2 was measured in gas inclusions in gneisses at the same locality (Zgonnik, 2020). Nivin (2019) reported H_2 concentrations up to 58 vol. % in free gases collected in underground mines of the Khibiny and Lovozero alkaline massifs located at $\sim$ 40 km to the south of the Olenegorsk mine. Anomalously high H_2 concentrations were also measured in the Kola superdeep borehole (SG-3) (Zgonnik, 2020) drilled in its shallow part through 7 km of Proterozoic rocks of the Pechenga belt (Pavlenkova, 1992). Kalinin et al. (2019) described gold mineralization associated with carbonation in the Pechenga Greenstone belt. The presence of methane and other light hydrocarbons was also detected in the Cuiab gold mine in the Archean Rio das Velhas Greenstone Belt (Magalhaes et al., 2020). The orebodies are hosted in $\sim$ 50 m thick carbonate-rich rocks ("lapa seca"; Vial et al. (2007)). H_2 was detected at relatively low level ($<$ 3 %) in fluid inclusions occurring in gold-bearing quartz-carbonate veins from the Mana district (Burkina Faso; Gaboury (2013)) and the central segment of the Keraf suture (Sudan; Gaboury et al. (2020)). These gold deposits are hosted in the Paleoproterozoic Hound belt and the Neoproterozoic Nubian shield, respectively. In the Neoproterozoic Bohemian massif (Czech Republic), quartz from the Libice orogenic gold deposit hosts uncommon fluid inclusions rich in H_2 ($<$ 6 mol. %) and bicarbonates (Hrstka et al., 2011). CH_4 content variability in the inclusions is interpreted as related to post-entrapment H_2 diffusion into the fluid inclusions.

We did find a natural hydrogen gas - gold deposit association not only in Precambrian rocks but also in Phanerozoic terranes. Ward (1933) reported H_2 concentrations up to 84 % in a borehole drilled in the Otway basin (Southern Australia and Victoria, Australia). The Paleozoic gold deposits in Victoria are found in turbidites of the Lachlan orogeny. Fe-carbonate poikiloblasts (so called "carbonate spots") were historically considered as indicators of gold deposition. They ubiquitously occur in less than $\sim$ 50 m wide zone around the deposits (Dugdale et al., 2009). Ward (1933) also reported up to 69 vol. % of H_2 in a borehole drilled on the Kangaroo Island where gold has also been mined in Cambrian formations (Kohinoor and Grainger's mine). In New Zealand, H_2-rich fluid inclusions ($<$ 8 mol. %) were described in the Mesozoic Otago Schists commonly containing Fe-carbonates (MacKenzie et al., 2007; Gaboury et al., 2021). High H_2 concentrations were measured in the Taseevskoe gold mine and in the Baleysky graben (Russia; Zgonnik (2020)) belonging to the Balei gold-bearing ore-system of Cretaceous age (Spiridonov et al., 2010). Gold-bearing veins in Balei ore-system can contain up to 20 % of Fe-carbonates. Gas analysis in the Ural superdeep drilling (SG-4) revealed the presence of more than 50 vol. % of H_2 (Zgonnik, 2020). The Uralian belt is known to host numerous Paleozoic gold deposits, some of them are associated with carbonation (Sazonov et al., 2001). Letnikov and Narseev (1991) described H_2-rich fluid inclusions in the Bestobe gold mine in the Charsk gold belt formed during Late Ordovician (North Kazakhstan; Goldfarb et al. (2014)). The presence of H_2 was also reported in fluid inclusions in quartz from a gold deposit located in the Shandong Peninsula (Zhili et al., 1989). Carbonation associated with gold deposition was described in this latter Mesozoic deposit (Liu et al., 2021).

The above review highlights a clear spatial relationship between anomalously high H_2 concentrations and gold deposits in terranes of all ages. To confirm this relationship, we track in the following the presence in gold provinces of geomorphological features, known as markers of H_2-bearing gas venting.

3. Ground depressions in the vicinity of orogenic gold deposits

Ground depressions occurring in sedimentary basins have been proposed as an H_2 exploration tool (Moretti et al., 2021) since some of them revealed H_2 concentration at the 1000 ppm level in the soil porosity (Zgonnik et al., 2015). The typical H_2-bearing ground depressions are barren, circular or elliptical and can be oriented. The use of ground depressions for H_2 exploration only requires satellite images and thus provides an easy identification of potential areas with H_2 seepage. Here, we focused on the identification of ground depressions located in the vicinity of orogenic gold deposits. First, based on literature data, we identified among recognized H_2-emitting depressions those located near gold deposits. In a second step, geomorphological features that resemble ground depression were searched for in gold provinces using satellite images provided by GoogleEarthPro^{TM}. The results of this section are summarized in Table 1. Satellite images of all the investigated ground depressions are also available in supplementary file F1. A *.kmz* file displaying all the localities discussed in the following is also provided as a supplementary material. An occurrence number (ON°) was attributed to each locality to simplify their description (Table 1).

ON°	Continent	Country	Ground depressions					Gold deposit						
			Location	Latitude	Longitude	Shape	Karst	Geological unit	Gold deposit/mine name	Age	Latitude	Longitude	D (km)	References
1	Africa	Madagascar	Maevatanana	15°54'43"S	47°21'57"E	Circular	Yes	Tsaratanana sheet	Kelimaizina	Archean	16°39'45"S	47°14'59"E	∼ 50	Rambeloson (1999); Yang et al. (2017)
2		Madagascar	Ambia	22°24'10"S	46°12'22"E	Circular	Yes	Bekily belt	West Ambia	Proterozoic	22°21'56"S	46°10'54"E	0	Rambeloson (1999)
3		Mali	Gassola	13°11'56"N	6°14'39"W	Circular	No	Birimian rocks	Kalana, Syama, Morila	Proterozoic	11°41'19"N	6°50'42"W	∼ 190	Lawrence et al. (2016)
4		South Africa	Johannesburg	26°11'56"S	27°38'38"E	Circular	Yes	Kaapvaal craton	South Deep, Mponeng, Kalahari Goldridge	Archean	26°24'53"S	27°40'30"E	0	Hammond and Moore (2006), Adomako-Ansah et al. (2017)
5		Tanzania	Sekenke	4°17'59"S	34°7'20"E	Circular	No	Tanzania craton	Sekenke	Archean	3°57'4"S	34°14'49"E	< 50	Mpangile et al. (2020)
6		Tanzania	Mara	1°28'0"S	34°27'40"E	Circular	No	Tanzania craton	North Mara	Archean	1°28'22"S	34°30'10"E	0	Kuehn et al. (1990)
7	America	Argentina/Bolivia	Juyuy Province	22°48'6"S	66°47'15"W	Circular	No	Sierra de Rinconada	Minas Azules, Farillon	Paleozoic	21°57'54"S	66°2'19" W	45-100	Ford et al. (2015)
8		Bolivia	Eastern Province	18°26'14"S	66°26'40"W	Square	No	Eastern Cordillera	Amayapampa	Paleozoic	18°28'37"S	66°22'51"W	< 10	Arce-Burgoa and Goldfarb (2009)
9		Brazil	Sao Francisco	16°26'52"S	45°14'0"W	Circular	Yes	Quadrilatero Ferrifero	Morro Velho, Sao Sebastiao	Archean	19°58'46"S	43°50'58"W	∼ 300	Vial et al. (2007); Soares et al. (2018)
10		USA	San Joaquin Valley	36°35'52"N	119°22'19"W	Square	No	Sierra Foothills	Mother Lode, Coulterville, Grass Valley	Mes.-Cen.	37°42'51"N	120°11'48"W	< 50	Marsh et al. (2008); Bohlke and Kistler (1986); Taylor et al. (2021)
11		Colombia	Caldas State	5°38'52"N	75°38'2"W	Circular	No	Calima Terrain	Marmato Mining District	Cenozoic	5°28'28"N	75°36'0"W	20	Tassinari et al. (2008)
12		Colombia	Puerto Libertador	7°50'4"N	75°41'30"W	Circular	No	Western Cordillera	Buritica, San Matias Copper-Gold-Silver Project	Cenozoic	7°11'47"N	75°20'33"W	< 80	Lesage et al. (2013)
13		Dominican Rep.	La Cueva	19° 2'55"N	70°2'18"W	Circular	No	Eastern Cordillera	Pueblo Viejo	Mesozoic	18°56'28"N	70°10'48"W	20	Sillitoe et al. (2006)
14		USA	South Carolina	34°48'13"N	78°39'24"W	Circular	Yes	Carolina slate belt	Barite Hill, Haile	Paleozoic	34°35'22"N	80°31'46"W	< 50	Foley et al. (2001)
15	Asia	China	Shandong	37°13'27"N	121°0'35"E	Circular	No	Shandong Province	Sanshandao,Dayin'gezhuang, Hushan, Songjuagou	Mesozoic	37°7'8"N	121°22'5"E	< 40	Liu et al. (2021)
16		China/Russia	Heilongjiang/Amur	49°30'20"N	129°14'27"E	Circular	No	Northern Lesser Khingan	Dong'an, Gaosongshan	Mesozoic	49°8'46"N	128°36'17"E	60	Zhang et al. (2019)
17		China/Russia	Amur oblast	52°15'36"N	127° 8'26"E	Circular	No	Northern Greater Khingan	Tianwangtaishan, Pangkaimen	Mesozoic	51°57'16"N	126°10'35"E	< 80	Zhang et al. (2019)
18		India	Karnataka	15°49'13"N	76°14'31"E	Square	No	Dhawar craton	Hutti, Buddini	Archean	16°12'22"N	76°38'45"E	0 - 50	Pandalai et al. (2003); Sarma et al. (2008)
19		India	Karnataka	15°29'51"N	75°37'48"E	Square	No	Dhawar craton	Gadag gold field	Archean	15°25'25"N	75°37'52"E	0	Sarangi et al. (2012); Swain et al. (2015)
20		Kazakhstan	Akmola	53°23'56"N	68°59'19"E	Circular	No	Kokshetau-Morth Tien Shan	Altyntau-Kokshetau, Raigorodok gold deposit	Paleozoic	53°26'10"N	69°15'8"E	0	Kovalev et al. (2018)
21		Myanmar	Khantha	23°43'10"N	95°54'17"E	Square	No	Sagaing fault zone	Kyaukpahto	Cenozoic	23°48'4"N	95°56'32"E	< 10	Swe et al. (2017)
22		Russia	Chelyabinsk oblast	54°25'53"N	61°32'39"E	Circular	Yes	Uralian belt	Kochkar, Svetlinskoe	Paleozoic	54°21'10"N	60°53'51"E	< 50	Belogub et al. (2017); Snachev et al. (2020)
23		Russia	Transbaikal	51°18'3"N	115°50'41"E	Circular	No	Balei ore field	Taseevskoe, Baleiskoe	Mesozoic	51°33'6"N	116°38'15"E	60	Spiridonov et al. (2010)
24		Uzbekistan	Navoiy	42°24'30"N	64° 0'23"E	Circular	No	Besopan Suite	Uchkuduk, Muruntau	Paleozoic	42°15'30"N	63°55'0"E	20	Drew et al. (1996); Wilde et al. (2001)
25	Europe	Spain	Zamora province	41°1'42"N	6°10'55"W	Circular	No	Iberian Hercynian Massif	Peralonso, Cabeza del Caballo, Pino del Oro	Paleozoic	41°1'56"N	6°13'21"W	0	Spiering et al. (2000)
26		Ukraine	Kryvyi Rih	47°36'35"N	33°13'52"E	Circular	Yes	Ukrainian Shield	Kryvyi Rih	Proterozoic	47°40'39"N	33°13'19"E	< 5	Berezovsky et al. (2021)
27	Oceania	Australia	Western Australia	33°10'34"S	119°46'21"E	Circular	No	Yilgarn craton	Kalgoorlie, Griffin's find, Golden Mile	Archean	30°45'38"S	121°33'6"E	0	Mueller and Groves (1991); Bateman and Hagemann (2004)
28		Australia	Western Australia	32°47'50"S	116°30'23"E	Square	No	Yilgarn craton	Boddington	Archean	32°45'38"S	116°22'27"E	4	Mueller and Groves (1991); Bateman and Hagemann (2004)
29		Australia	Yorke Peninsula	34°55'48"S	137°40'31"E	Circular	Yes	Olympic Domain	Hillside	Proterozoic	34°31'49"S	137°52'13"E	30-40	Cerlienco (2009)
30		Australia	Victoria	37°27'30"S	143°36'10"E	Irregular	No	Lachlan Belt	Ballarat	Paleozoic	37°35'28"S	143°51'14"E	0	Dugdale et al. (2009)
31		New Zealand	Otago	45° 7'56"S	170° 2'20"E	Circular	No	Otago Schist	Macraes	Mesozoic	45°22'6"S	170°26'49"E	0	MacKenzie and Craw (2007); MacKenzie et al. (2007)
32		New Zealand	Tasman	40°58'19"S	172°49'2"E	Circular	No	Western province	Sams Creek	Paleozoic	41° 3'56"S	172°45'20"E	< 10	Christie and Brathwaite (2003)

Table 1: List of the studied ground depressions in sedimentary basins overlying gold deposits. Abbreviations are as follows: ON°, occurrence number; Karst, occurrence in a karst region; D (km), distance between the ground depressions and the orogenic gold deposit in km; References, references describing the gold deposit and the presence of Fe-carbonates when mentioned.

Except for Russia (Sukhanova et al., 2013; Larin et al., 2015), all the previously reported H_2 emitting ground depressions are located in the vicinity of gold provinces. In the USA (ON°14), H_2 was measured in ground depressions, parts of the Carolina Bays (Zgonnik et al., 2015), and extending on the Atlantic Coastal Plain overlying the Carolina slate belt (Alarifi et al., 2021). The Carolina slate belt is composed of Cambrian volcanic and sedimentary rocks hosting numerous gold deposits found in alteration zones containing carbonates (Foley et al., 2001; Klein et al., 2007). Carolina Bays are found at less than ~ 50 km from the Brewer and Haile gold mines (Figure 2 A and B). The ground depression described in Prinzhofer et al. (2018) in Mali (ON°3) occurs in the Taoudeni sedimentary basin which is bordered by numerous Paleoproterozoic Greenstone belts hosting world-class orogenic gold deposits (Lawrence et al., 2013; Koné et al., 2021). The Sao Francisco basin (Brazil) in which H_2 emissions were detected in ground depressions and monitored (ON°9; Prinzhofer et al. (2019)) is also surrounded by Greenstone belts including the Archean Rio das Velhas Greenstone Belt. As discussed above, this latter formation hosts gold mines in which methane and other light hydrocarbons were analyzed (Magalhaes et al., 2020). Finally, H_2 was detected in the soil of ground depressions in the Yilgarn craton known to host numerous world-class orogenic gold deposits (Australia; ON°27; Frery et al. (2021); Mainson et al. (2022)). Frery et al. (2021) studied ground depressions along the Darling fault separating the Perth basin from the Yilgarn craton. Mainson et al. (2022) measured up to 400 ppm of H_2 in a ground depression located near gold mines in the northwest of Kalgoorlie. Excluding O_2 and N_2 mainly associated with air contamination, H_2 is found to be associated with CO_2 and CH_4 in the gas analyses in soils from ground depressions in the USA (ON°14; Zgonnik et al. (2015)) and in Australia (ON°27; Frery et al. (2021)).

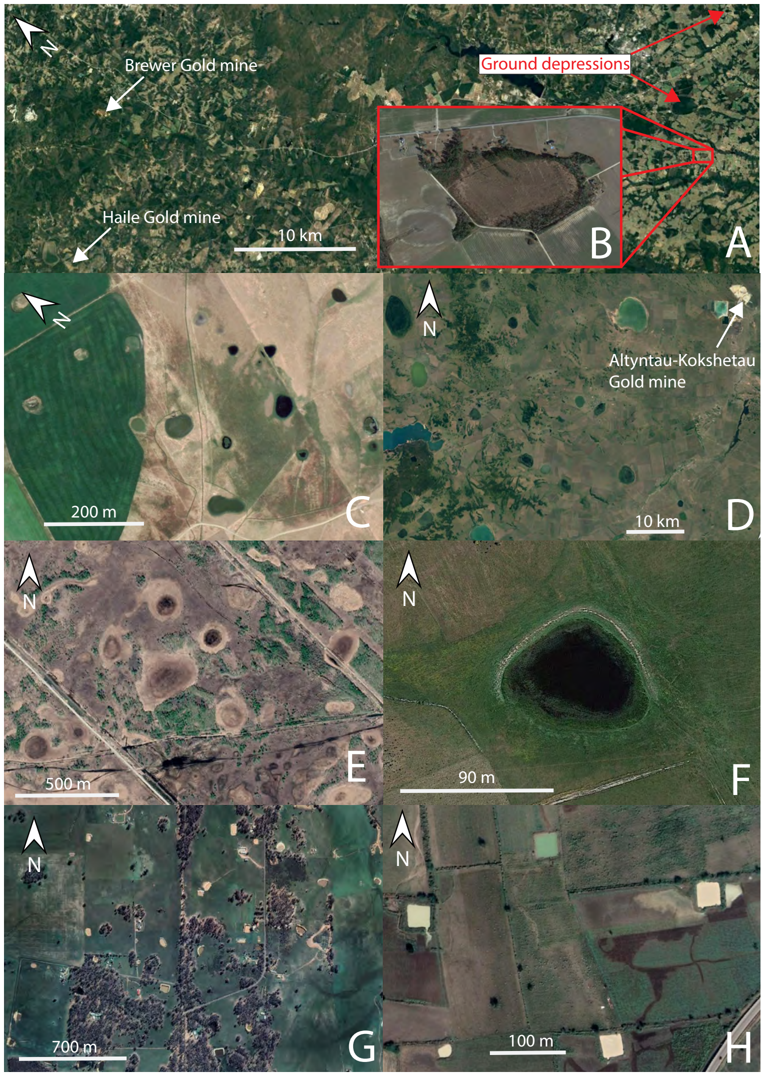

Figure 2: Satellite images of ground depressions in the vicinity of gold deposits. A and B: ovoid ground depressions (Carolina Bays) in South Carolina (USA) in the vicinity of the Brewer and Haile gold mines, the Paleozoic Carolina slate belt (ON°14; location 34°28'21"N 80°19'36"W). C: circular ground depressions in alluvial sediments of Ida valley overlying the Mesozoic Otago Schists (ON°5; location: 45°12'42"S 169°38'7"E). The image was taken 10 km to the southeast of the Ophir deposit (Blundell et al., 2019). D: elliptical large ground depressions in North Kazakhstan near the Altyntau-Kokshetau gold mine (ON°20; location: 53°10'29"N 68°35'52"E). E: circular, barren ground depressions in the Amur oblast at 60 km to the northeast of the Northern Greater Khingan gold deposit (Zhang et al. (2019); ON°17; location: 52°16'12"N 127°9'23"E). F: semi-circular depression in northeast Spain, 3 km east of the Pino del Oro village (ON°25; location: 41°35'7"N 6°4'58"W). G: irregular shaped ground depressions in Victoria (Australia) near the city of Bendigo (ON°30; location: 36°44'12.37"S 144°36'2.08"E). The open pit gold mine of Fosterville is located at 8 km to the west. H: squared-shape depressions in the city of Gadag (India) where an orogenic gold deposit occurs (Sarangi et al., 2012).

We have shown that H_2- (and CH_4-) rich gases have been reported in several orogenic gold-deposits. Furthermore, five out of six areas where H_2-emitting depressions have been unequivocally reported are located in the vicinity of geological formations that host orogenic gold deposits. Assuming that ground depressions are possible H_2-emitting centers, we further investigated the presence of geomorphological features in sedimentary basins related to gold provinces with satellite images.

Many processes unrelated to H_2 emissions can lead to the formation of ground depressions. Sinkhole formation in karsts, thermokarst lake formation in permafrost and glacier erosion are among the main contributors to the formation of natural ground depressions. Canada, Alaska, Northern Europe and North Russia were thus excluded from the ground depression search despite the fact that these regions/countries host some of the largest gold deposits on Earth (Figure 1). Karst regions were also avoided as much as possible based on the world karst aquifer map (Goldscheider et al., 2020). Geomorphological features of interest were identified based on the presence of a high density of structures having similar shapes, the absence of vegetation or the filling of the depressions with water. Screening was restricted to within 100 km of known orogenic gold deposits.

Including the four localities discussed above, ground depressions were identified near world-class gold deposits in 32 localities distributed over 20 countries on five continents (Table 1 and Figure 1). Among them, two occurrences in the Yorke Peninsula (Australia; ON°29) and in the Witwatersrand basin (South Africa; ON°4) have already been reported as possible ground depressions associated with H_2 emission (Moretti et al., 2021; Geymond et al., 2022). There are thus 26 new occurrences reported here. The ground depressions are found in sedimentary basins (mainly alluvial deposits) over areas spanning from less than 20 km^2 in New Zealand (ON°32) and Ukraine (ON°26) to more than 10 000 km^2 in South Africa (ON°4), the USA (ON°14), Western Australia (ON°27) and Russia (ON°22). Ground depressions vary in size from less than 50 m in diameter in Tanzania (ON°6), Bolivia (ON°8), Dominican Republic (ON°13), India (ON°18 and 19), Myanmar (ON°21), Spain (ON°25), Western Australia (ON°28) and New Zealand (ON°31 and 32), to several kilometers in diameter in Western Australia (ON°27), Victoria (ON°29), Mali (ON°3), North Kazakhstan (ON°20), South Carolina (USA; ON°14) and the South Urals (ON°22). Large- and medium-sized depressions are circular or elliptical and systematically associated with smaller depressions (Figure 2 A, B and D). Some localities only contain small depressions (< 50 m; ON°6, 8, 13, 18, 19, 21, 24, 25, 28, 31 and 32). In this latter case, the size is homogeneous with a diameter of ~ 40 m for all the localities. Moreover, elevation profiles across small depressions revealed that their whitish margins can be elevated leading to M shape cross-section profiles (ON°25, 28 and 30). A great variability in shape is also observed among these small depressions with semi-circular shapes in Tanzania, Dominican Republic, New Zealand, Spain and Uzbekistan (Figure 2 C and F), irregular shapes in Victoria (Australia; Figure 2 G), and squared shapes in Western Australia (ON°28), Myanmar, California and India (Figure 2 H).

Small irregular-shaped depressions similar to those observed in Victoria were also observed on Kangaroo Island (Australia).

Fifteen, eleven and six occurrences of ground depressions are located at less than 10 km, in-between 10 and 50 km, and at more than 50 km from a known gold deposit, respectively. Depressions were observed near some of the largest known gold deposits (Figure 1; Goldfarb et al. (2001)) including the Witwatersrand basin (South Africa, ON°4), the Shandong Peninsula (China, ON°15), the Uralian belt (ON°22), the Kyzylkum desert (Uzbekistan, ON°24), and the Yilgarn craton (Australia, ON°27 and 28). They also occur in historical gold provinces such as in northwestern Spain where gold is extracted since the pre-Roman era (ON°25; Sánchez-Palencia et al. (2018)), and places known for major gold rushes in the 1850s such as the Sierra Nevada foothills (USA, ON°10), Victoria (Australia, ON°30) and Otago (New Zealand, ON°31). Gold mineralization in the deposits associated with geomorphological features spans over 3 billion years from Archean with the oldest deposits in the Tanzania craton (ON°5 and 6) and the Quadrilatero Ferrifero (Brazil; ON°9) to Cenozoic with the youngest deposits in Myanmar (ON°21) and Columbia (ON°11 and 12). The host rocks of the gold deposits studied here display a wide variety of composition including banded iron formations, volcanic rocks and carbonaceous sediments. For all the studied occurrences where data are available, carbonates were described in association with gold mineralization (Table 1 and references therein).

4. High density of self-organized white spots in the vicinity of orogenic gold deposits

In addition to ground depressions, we also screened satellite images in the vicinity of gold deposits for the presence of geomorphological features at the small scale. A high density of circular structures without visible vegetation less than 20 m in diameter, separated from each other by distances of less than 50 m, is observed in semi-arid regions near gold mines (Figures 1 and 3). Some of these structures are located near ground depressions and gold deposits such as in Madagascar (ON°2), Mali (ON°3; Prinzhofer et al. (2018)), Tanzania (ON°5 and 6), Myanmar (ON°21) and Australia (ON°27 and 28). In Mali, they are also found $\sim$ 2 km west of the Bourakbougou village where gas with 98 % of H_2 has been measured in a series of wells (Prinzhofer et al., 2018). In Tanzania, high density of white spots are common and occur near the gold mines of Golden Pride, Bulyanhulu, and Buzwagi. In this latter case, white spots are found to enlarge towards the northeast of the gold mine where surficial structures resemble ground depressions observed elsewhere (Figure 3 C). White spots with asymmetric shapes and a long tail leading to a comet shape are observed at less than 30 km from the North Mara gold mine in Tanzania, at less than 10 km to the east of the Turk gold mine in Zimbabwe and at less than 3 and 10 km to the southwest and to the south of the Taparko-Boroum and Kalsaka gold mines in Burkina Faso, respectively (Figure 3 D). These comet-shaped white spots have a group organization leading to a "peacock feather-like" appearance described in Glover et al. (1964). In Madagascar, Zimbabwe and Burkina Faso, these patterns have been found in the vicinity of small (< 5 m) white circular spots, suggesting a common origin for the two geomorphological features. Finally, we discovered a high density of small (< 10 m) circular structures, again without apparent vegetation, in Western Australia, in the Yilgarn craton (Figure 4). A darker thin rim outlines these structures in Mali and Australia. The geomorphological structures are extremely common and found in a region with numerous gold mines exploiting deposits found in Archean Greenstone Belts (Figure 4).

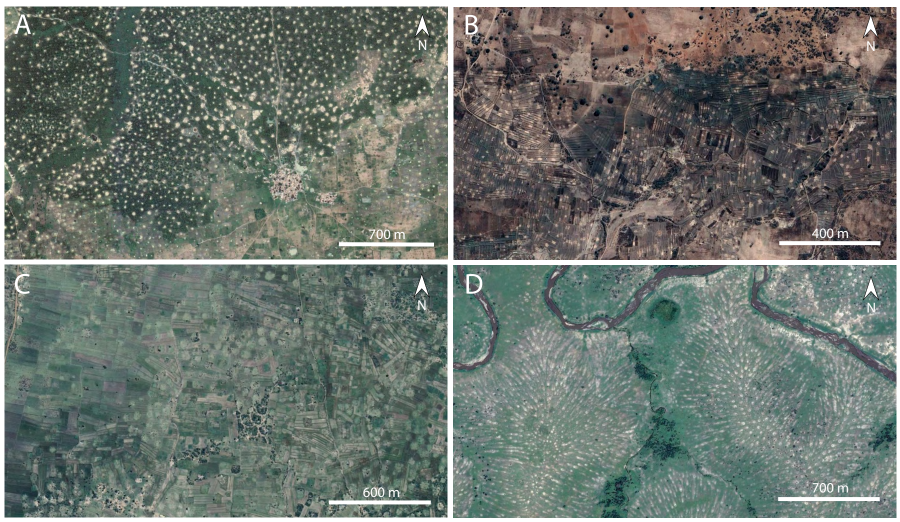

Figure 3: Satellite images of areas with a high density of small (< 20m) barren circular white spots in various gold provinces. A: white spots in Mali, ∼ 7 km to the east of the ground depression described in Prinzhofer et al. (2018) (13°13'18"N, 6°10'17"W). B: white spots in Tanzania bordering the Golden Pride gold mine (4°5'46"S, 33°12'54"E). C: ground depressions located north of the white spots shown in B (Tanzania) near the Buzwagi gold mine (3°47'12"S, 32°47'3"E). D: whitish barren spots displaying a comet shape organized in the manner of "peacock feathers" in Tanzania, 25 km to the east of the North Mara gold mine (ON°6; 1°35'24"S, 34°41'41"E). The tails of the comet-shaped barren spots are oriented downslope.

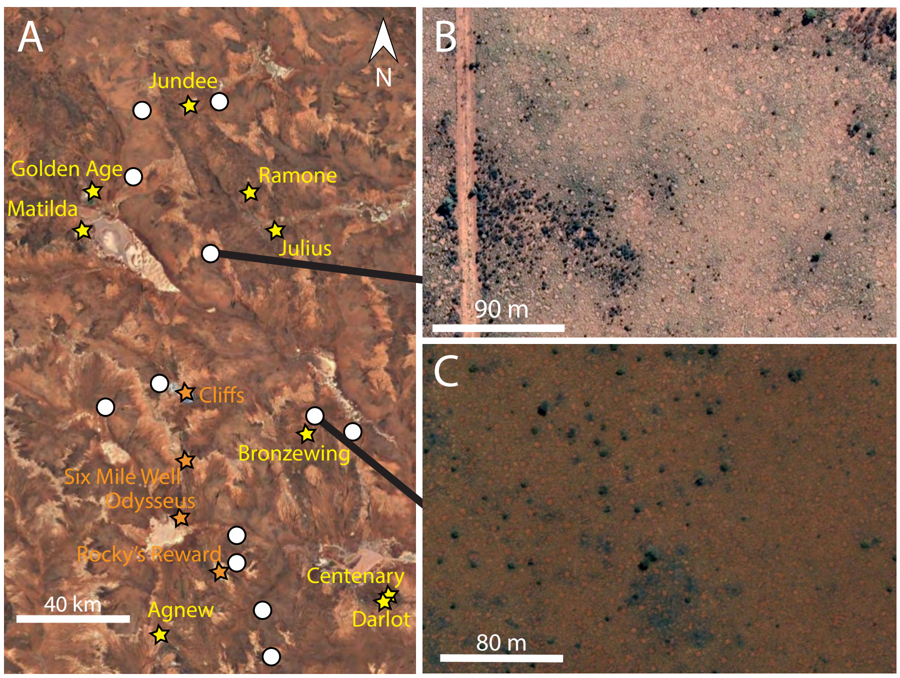

Figure 4: Satellite images of areas with a high density of < 10 m wide barren circular structures in Western Australia (26°49'33"S, 120°40'28"E). A: Satellite image showing the location of the geomorphological structures (white dots) and of the mines (yellow and orange stars for Au and (Cu,Ni) mines, respectively). B and C: Close view of the structures, showing the presence of a dark rim probably associated with a vegetation density higher than in the matrix.

Point pattern analysis is a common tool in geomorphology and ecology to better characterize the spatial relationship between surface features, and thus to better constrain their origin (Hammer, 2009; Getzin et al., 2015). We digitized small barren geomorphological features on satellite images collected near gold mines in Australia, Mali and Tanzania to determine their density, and the mean of the distance from each spot to its nearest neighbor (or mean nearest neighbor distance; Table 2). We measured the lowest and the highest densities of 3 and 79 geomorphological features per ha in Mali and Australia, respectively. The mean nearest-neighbor distance is the shortest with 8 m in Australia, and approximately four times higher in Mali and Tanzania (Table 2). The x,y-positions were also processed with advanced point patterns methods allowing to probe pattern organization over a wide range of scales (Table 2). We first used Voronoi tessellations to determine the surrounding area which is the closest from each feature with barren soil (Voronoi cell). A regular pattern is expected to be composed of Voronoi cells with 6 corners. We thus determined the mean number of corners of the Voronoi cells and the fraction of cell with 6 corners to estimate the regularity of the pattern. We also used the pair-correlation function ($g(r)$) providing the density in geomorphological features at a distance r of a reference point (Figure 5). $g(r) = 1$ for complete spatial randomness (CSR), $g(r) > 1$ for aggregated features, and $g(r) < 1$ for dispersed features. The analyses were performed with the Spatstat package of the R-software (Baddeley and Turner, 2005). At all investigated localities, Voronoi cells with 6 corners dominate and represent 42, 41 and 34 % of the cells in Australia, Mali and Tanzania, respectively (Table 2). The pair-correlation function systematically display low values at short distance. For Australia and Mali, it also displays a peak at high value ($g_{max} > 1.27$ in Mali and Australia) at a distance slightly higher than the mean nearest-neighbour distance (Figure 5). This indicates that the white spots described here are organized in periodic patterns.

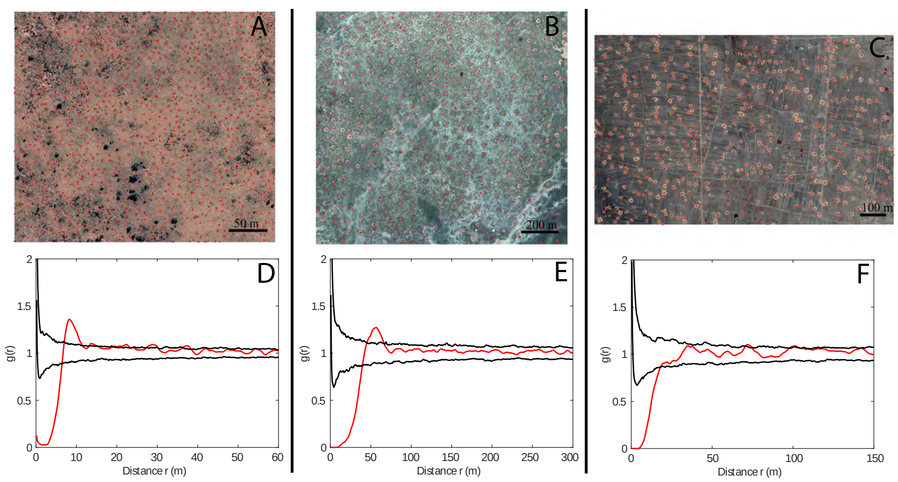

Figure 5: Results of spatial point pattern analysis with pair-correlation function in Australia (A and D), Mali (B and E) and Tanzania (C and F). A, B and C: Satellite images with mapped barren geomorphological features (red dots). D, E and F: Pair-correlation function ($g(r)$; red line) as a function of distance for the spatial patterns displayed in A, B and C, respectively. The black lines indicate the 5th-lowest and 5th-highest value of 200 complete spatial randomness (CSR) simulations.

Location	Fe-carbonate	Name of nearby mine(s) or carbonatite	Latitude	Longitude	N	Density (ha^{-1})	n° sides	fraction (%)	NND (mean/median, m)	g_{max}	D_{gmax} (m)	Ref.
Australia (Yilgarn)	Gold deposit	Matilda, Jundee, Bronzewing, Agnew	26°49'40"S	120°40'9"E	776	79	5.97	42	7.9/7.6	1.36	8	
Mali	Gold deposit	Kalana, Syama, Morila	13°12'34"N	6°6'44"W	469	3.0	5.94	41	44/43	1.27	57	
Tanzania	Gold deposit	Bulyanhulu, Buzwagi, Golden Pride	3°58'56"S	33°13'21"E	507	5.9	5.93	34	25/23	1.0982	72	
Australia (Pilbara)	BIF	Mount Whaleback	23°28'16"S	119°51'17"E	2108	55	5.98	46	11/11	1.52	13	[1]
Brazil	Carbonatite	Angico dos Dias	9°35'54"S	43°26'11"W	881	18	5.97	42	18/18	1.37	22	
Malawi	Carbonatite	Chilwa Island	15°5'58"S	35°33'5"E	1139	8.1	5.97	33	23/22	1.16	38	
Namibia	Carbonatite	Dicker Willem	26°27'49"S	16°2'1"E	433	47	5.94	39	11/11	1.21	14	
South Africa	Carbonatite	Zandkopsdrift	30°47'47"S	18°3'6"E	770	2.4	5.97	46	47/45	1.327	58	
South Africa	Carbonatite	Palabora	23°51'26"S	31°10'56"E	316	2.7	5.94	41	40/38	1.84	42	
Pockmark fields												
North Sea (Troll area)			61°N	4°E	3054	0.087	5.98	32	203/189	1.07	197	[2]
Monterey Bay (Big Sur)			35°45'N	121°45'W	489	0.0564	5.95	39	293/286	1.183	356	[3]
Nile Deep Sea Fan (Rosetta)			32N	30E	1423	3.6	5.96	30	27/24	1.4328	20	[3]

Table 2: Results of spatial point pattern analysis of the high density of barren white spots near orogenic gold deposits, banded iron formations (BIF) and carbonatites. The point pattern analysis of three previously published pockmark fields was also performed for comparison. [1]: Getzin et al. (2016); [2]: Hammer (2009); [3]: Cartwright et al. (2011)

5. Discussion

5.1. *Spatial link between geomorphological features, H_2 gas occurrence and orogenic gold deposits*

Ground depressions have been proposed as markers of H_2 emissions and as a tool for H_2 exploration (Moretti et al., 2021). It appears that among the six studies which described ground depressions with H_2 emission, five were conducted in the vicinity of gold deposits (Zgonnik et al., 2015; Prinzhofer et al., 2018, 2019; Frery et al., 2021; Mainson et al., 2022). Moreover, the ground depressions observed here in South Africa (ON°4), China (ON°15), Russia (ON°23), Ukraine (ON°26), Australia (ON°27 and 28), New Zealand (ON°31) and on the Kangaroo Island (Australia) are located in sedimentary basins overlying gold deposits where high H_2 concentrations have been previously measured (Ward, 1933; Zhili et al., 1989; Sherwood Lollar et al., 2014; Zgonnik, 2020; Gaboury et al., 2021; Boreham et al., 2021). Thousands of ground depressions were identified here in the vicinity of gold deposits in 26 new localities.

In addition to the ground depressions mentioned above, we identified small (< 20 m in diameter) circular spots of barren soil with a high density up to 80 ha^{-1} which are also located near gold mines in semi-arid regions. Such geomorphological features had not been linked to hydrogen emission until now. However, they recall by their size, density and shape, the fairy circles described in Namibia, South Africa, Angola and Australia (Getzin et al., 2021a; Meyer et al., 2021). Getzin et al. (2021b) proposed three criteria to define fairy circles: the absence of vegetation, their occurrence in semi-arid regions and their organization into periodic patterns. The spots described here all meet the first two conditions. Spatial point pattern analysis also reveals that they are not randomly organized with a predominance of Voronoi cells with 6 corners and pair-correlation functions with low values at low distance. In Australia and Mali, $g(r)$ displays a clear peak at a distance slightly above the mean nearest-neighbour distance, indicating self-organization with a constant wavelength of the pattern. The geomorphological features described here in Australia and Mali can thus be classified as fairy circles according to the criteria defined by Getzin et al. (2021b). This is consistent with the darker rim of the structures observed here in Australia and Mali (Figure 3), suggesting preferential vegetation development at their margin as it is observed in fairy circles. Vegetation banding, a particular class of vegetation pattern consisting in vegetation separated by bands of barren soil, was previously described in the same region than the fairy circles of the Yilgarn craton reported here (Mabbutt and Fanning, 1987).

The present review provided 34 examples of gold mines or gold deposits in which gas, water or fluid inclusions display unusually high H_2 concentrations. The presence of H_2 in fluid inclusions should be interpreted with care since it could be related to two events. H_2 could indeed be trapped during inclusion formation in the presence of the metamorphic fluid involved in gold deposition. Alternatively, the fluid inclusion composition could be modified after entrapment due to later hydrogen diffusion into the inclusion (Mavrogenes and Bodnar, 1994; Hrstka et al., 2011; Goldfarb and Groves, 2015). As a result, high H_2 concentrations in fluid inclusions in gold deposits could reflect post-entrapment H_2 production, which is a process of interest here. The reports of high H_2 concentrations in Precambrian rocks and associated sedimentary basins are almost exclusively related to gold deposits. One notable exceptions consist in measurements in Kansas (Newell et al., 2007). Banded iron formations and ultramafic/mafic rocks have been proposed as a potential source rock for H_2 in Precambrian rocks (Sherwood Lollar et al., 2014; Geymond et al., 2022). They are common host rocks for gold deposits in Archean greenstone belts due to their high Fe content favoring sulfidation (Phillips and Powell, 2010). We showed here the close spatial relationship between H_2 emissions and the presence of banded iron formations or mafic/ultramafic rocks hosting gold deposits in South Africa (ON°4), Tanzania (ON°5 and 6), Brazil (ON°9), California (ON°10), India (ON°18 and 19) and Ukraine (ON°26). For these localities, we cannot unambiguously distinguish between the potential H_2 source rocks. Evidence for H_2 emissions are not restricted to banded iron formation and mafic/ultramafic rocks since ground depressions also occur in sedimentary rocks hosting gold deposits for example in the carbonaceous turbidites of Victoria (Australia, ON°30) and of the Otago Schists (New Zealand, ON°31). We found reports of H_2 emissions and ground depressions in terranes of both Precambrian and Phanerozoic ages (Figure 1; Table 1). Banded iron formations are almost exclusively restricted to Precambrian rocks (Klein, 2005) whereas orogenic gold deposit formation spans the whole Earth's crust history (Figure 1; Goldfarb et al. (2001)). The age of rocks at the studied localities thus confirms that one of the main common denominator of H_2 emissions in continental rocks is the presence of orogenic gold deposits. Potential geochemical processes that could explain the clear spatial link between H_2 emissions and gold deposits are discussed in the next section.

5.2. Towards a prominent role of Fe-carbonate dissolution

Based on the study of ultramafic rocks, iron-bearing minerals are considered as good candidates for H_2 production during fluid-rock interaction. Sherwood Lollar et al. (2014) and Boreham et al. (2021) have proposed that serpentinization in Precambrian rocks is responsible for H_2 production. A classical component of Precambrian rocks indeed consists in Greenstone belts containing mafic and ultramafic rocks. However, the primary Fe^{2+}-bearing minerals (e.g. olivine, pyroxene) have extensively reacted during metamorphism and are generally not preserved, suggesting that other rock types may be involved in H_2 production. Geymond et al. (2022) recently proposed that H_2 production could occur in banded iron formations found in Archean Greenstone belts during magnetite weathering associated with hematite or goethite production. Nevertheless, thermodynamic calculations indicate that magnetite weathering should not produce significant amount of H_2. The magnetite-hematite equilibrium indeed implies a partial H_2 pressure of $\sim 10^{-5}$ bar at 25°C (Arrouvel and Prinzhofer, 2021). In addition to iron oxides, the main ferrous minerals in iron formations are Fe-carbonates including siderite ($FeCO_3$), ankerite ($CaFe(CO_3)_2$) and ferroan dolomite ($Ca(Mg,Fe)(CO_3)_2$). Their origin is related to burial diagenesis in anoxic environment (Bekker et al., 2010).

Orogenic gold deposits are also known to contain significant amount of Fe-carbonates. The commonly admitted model of orogenic gold deposit formation involves three steps (Phillips and Powell, 2010). First, metamorphic devolatilization of gold- and sulfur-bearing sediments and mafic rocks occur in subducted oceanic slabs at $\sim 500°C$ (greenschist to amphibolite facies transition). The released H_2O-CO_2 fluid is buffered by the H_2CO_3/HCO_3^- equilibrium to slightly acidic conditions (Phillips and Powell, 2010) in which highly stable $Au(HS)S_3^-$ complexes are formed (Pokrovski et al., 2015). Auriferous fluids contain oxidized carbon and reduced sulfur and are thus moderately oxidized. They migrate upwards along shear zones and fractures. In some particular lithologies, their interaction with the wallrock induces gold deposition. Reaction with reduced carbonaceous sediments promotes auriferous fluid reduction and gold precipitation. The sulfidation of iron-rich rocks such as banded iron formations and mafic (e.g. dolerite) and ultramafic rocks also leads to Au precipitation. Sulfidation occurs in parallel with hydrothermal alteration of the wallrock forming assemblages typically composed of quartz, Fe-rich carbonate (i.e. siderite and ankerite), sericite and chlorite (Eilu and Groves, 2001). Fe-carbonates are described in all the areas studied here where petrological data are available (see references in Table 1), and thus appear as first-order candidates to produce H_2 during interaction with water. H_2 production during Fe-carbonate incongruent dissolution is expected to occur according to the following reaction:

$$3FeCO_3 + H_2O = Fe_3O_4 + 3CO_2 + H_2 \tag{1}$$

Considering a maximum fraction of 20 mol.% of siderite in gold deposits (Stromberg et al., 2018), reaction 1 could produce ~ 1 mole of H_2 per kg of rock. This maximum H_2 production corresponds to two times the maximum H_2 production expected for dunite serpentinization (0.45 mol/kg for the formation of magnetite with the ferrous iron of an olivine with a Fe/(Mg+Fe) ratio of 0.1). However, the presence of Fe^{2+} in a phase does not guaranty H_2 production in detectable amounts during fluid rock interaction for three reasons: 1) the reaction has to proceed fast enough to modify the fluid composition; 2) the reacting phase should not be stable at a low hydrogen activity. In other words, the thermodynamic driving force for reaction (1) should be sufficient to produce significant amounts of H_2 before reaching equilibrium (Arrouvel and Prinzhofer, 2021); 3) H_2 should not be totally consumed by other reducing reactions or biological activities.

Regarding 1), the dissolution rate of carbonates at pH = 8 is approximately 3, 4 and 5 orders of magnitude higher at 60°C than for olivine, quartz and chlorite, respectively (Black et al., 2015). Fe-carbonates are thus expected to be the most reactive phase in gold deposit. This is consistent with observations of preferential ankerite weathering in gold deposits, leading to orange to brown colors associated with the presence of ferri(hydr-)oxides (Craw et al., 2010; Stromberg et al., 2018; Cudby et al., 2021).

Regarding 2), thermodynamic calculations with Phreeqc indicate that reaction 1 can produce up to 0.9 mol/kg of H_2 at temperatures below 200°C (Supplementary material file F2). At low water to rock ratio, equilibrium is rapidly reached. Complete reaction requires water to rock ratios between 100 and 10000. H_2 production in gold deposits must occurs in open system conditions with important fluid circulation. H_2 is generally measured in highly permeable zones such as fractured rocks in gold mines (Lin et al., 2005), and sedimentary basins where the geomorphological features observed here were found. The need for significant fluid circulation to reach a high reaction progress may also explain why Fe-carbonates as old as Archean are still not completely reacted today (as it is the case for ultramafic rocks for example) and continue to produce H_2. Reaction 1 also produces significant amounts of CO_2. The systematic presence of CO_2 in association with H_2 in the gas collected in gold mines (Sherwood Lollar et al., 1993a; Boreham et al., 2021) and in the soils of ground depression found near gold deposits (Zgonnik et al., 2015; Frery et al., 2021) support a same geochemical origin for these gases. Zgonnik et al. (2015) measured a rather constant H_2:CO_2 ratio of 0.05 in their analyses of soil gases in ground depressions from South Carolina (USA). Larin et al. (2015) measured concentrations in CO_2 and H_2 at the thousands of ppm level in the soil of ground depressions in Russia. However, we found no orogenic gold deposits in the vicinity of these latter geomorphological features. This close link between H_2 and CO_2 was also observed during gas monitoring in boreholes located in the TauTona gold mine in the Witwatersrand basin (Lippmann-Pipke et al., 2011). H_2 concentrations peaks were found to be correlated with CO_2 concentration peaks only (no correlation with CH_4 and He) and with seismic activity. This was interpreted as evidence for the association of these two gases during transport enhanced by blasting activities.

Regarding 3), H_2 is not only systematically associated with CO_2 but also with CH_4 and light hydrocarbons in gas sampled near gold deposits (references in the above review). Carbon isotopic composition of gas collected in gold mines indicates an abiotic origin for these reduced gases (Sherwood Lollar et al., 2007, 2008; Boreham et al., 2021), through a reaction of the type:

$$CO_2 + 4H_2 = CH_4 + 2H_2O \tag{2}$$

Alternatively, CH_4 can be directly produced from Fe-carbonate in the presence of H_2 without CO_2 as an intermediate phase (carbonate methanation; Etiope and Sherwood Lollar (2013)).

Carbonaceous matter is also an ubiquitous phase in gold deposits with multiple origins including sedimentary deposition associated with host rock formation, and CO_2 reduction associated with gold mineralization (Hu et al., 2015, 2017; Chinnasamy and Mishra, 2017). Late siderite alteration has not been proposed as a forming process for carbonaceous matter in gold deposits. However, petrological observations suggest magnetite and graphite formation during siderite dissolution in Martian meteorites (Steele et al., 2012), metamorphic rocks from the Isua Supracrustal belt (Van Zuilen et al., 2003) and banded iron formations from Western Australia (Rasmussen and Muhling, 2018), according to the following reaction:

$$CO_2 + 2H_2 = C + 2H_2O \tag{3}$$

Milesi et al. (2015) experimentally reproduced this latter reaction in the 200-300°C range. The thermodynamic driving force for CO_2 reduction in carbonaceous matter, CH_4 and hydrocarbons is high, and H_2 concentrations are expected to be low at thermodynamic equilibrium (see Supplementary material file F2). However, such predictions are not consistent with the observations of several tens of percent of H_2 in gas collected in gold mines. Kinetic data reveal that abiotic methane and carbonaceous matter formations are sluggish reactions at temperatures below 300°C (McCollom and Seewald, 2001, 2003; Seewald et al., 2006; Milesi et al., 2015). Alloys, oxides and sulfides are mineral catalysts for Fischer-Tropsch type synthesis of methane (Horita and Berndt, 1999; Preiner et al., 2020). Such catalyst minerals may be present in gold deposits and the production of CH_4 and hydrocarbons is thus possible at temperature below 300°C. The presence of pyrite in gold deposits may consume H_2 during gold deposit alteration, according to the following reaction of pyrrhotite formation:

$$FeCO_3 + FeS_2 + H_2 = 2FeS + CO_2 + H_2O \tag{4}$$

Experiments have revealed that the $FeS_2 + H_2 = FeS + H_2S$ reaction can proceed in several days in the 90-180°C range under high H_2 pressure (Truche et al., 2010). Pyrite reaction will thus probably influence the H_2 yield of fluid-rock interaction in gold deposits. Major controlling factors will be the relative proportion and dissolution rate of Fe-carbonates and pyrite during alteration.

5.3. Model of H_2 production during gold deposit alteration

We attempt here to incorporate Fe-carbonate dissolution into existing models of gold deposit alteration in order to propose a general model of H_2 production under subsurface conditions (Figure 6).

In the near surface where oxidizing conditions prevail, meteoric water Fe-carbonate interaction does not produce H_2. Fe-carbonate alteration rather involves atmospheric O_2 consumption and ferri(hydr-)oxide formation.

In aquifer, Fe-carbonate oxidation progressively consumes O_2 as the fluids migrate downwards, leading to anoxic water transport (Figure 6; Grenthe et al. (1992)). In gold provinces, water can flow through ore deposits containing highly reactive Fe-carbonates which can dissolve at low temperature (< 150°C) to form magnetite, H_2 and CO_2 according to reaction 1 (Figure 6). Siderite is paramagnetic whereas magnetite is ferromagnetic, producing a strong magnetization. This is consistent with the observation of strong magnetic anomalies in sediment-hosted gold deposits such as those found in northwestern Spain (Ayarza et al., 2021) and in the Otago Schist (New Zealand; Blundell et al. (2019)). Naudé et al. (2011) also measured a concentration of magnetic minerals (probably magnetite) in the center of fairy circles. H_2 and CO_2 released during siderite dissolution can further react to form reduced carbon species (CH_4, hydrocarbons and carbonaceous matter; Figure 6). However, carbon

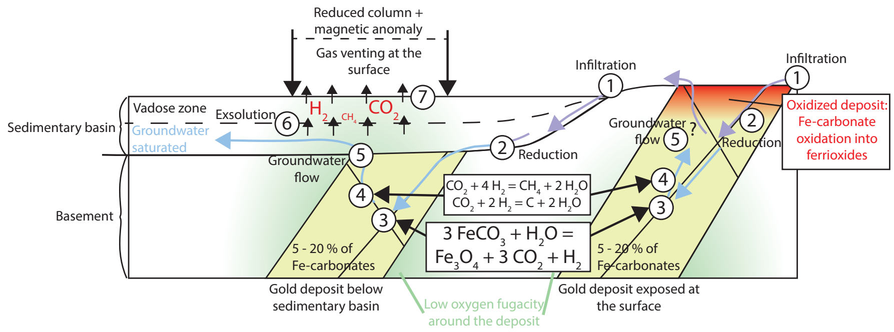

Figure 6: Schematic reduced column model considering Fe-carbonate dissolution/H_2 production, inspired by the model proposed in Cameron et al. (2004) for gold deposit alteration. The model considers alteration of gold deposits either concealed below a sedimentary basin (left) or exposed at the surface (right). It can be divided in the following steps: 1) Infiltration of water rich in O_2. This leads to gold deposit oxidation with ferri(hydr-)oxide formation when it is exposed at the surface. 2) Progressive water reduction along the flow path during fluid/rock interaction. 3) Alteration of the gold deposit containing Fe-carbonates leading to magnetite, CO_2 and H_2 production. This reaction is the main contributor to the reduced column model. It also induces a strong solid volume change of 50% with consequences for ground deformation. 4) Kinetically-limited CO_2 reduction by H_2. Reduced carbon phases including methane, carbonaceous matter and hydrocarbons are produced. 5) Dissolved H_2 and CO_2 transport in groundwater along fractures. Measurements of H_2, CO_2, CH_4 and hydrocarbons performed in underground gold mines probably sample such groundwater or a gas phase exsolving from groundwater. The fate of gases in exposed gold deposits is poorly constrained and requires further analysis with gas measurements at the surface. 6) Gas exsolution in sedimentary basin at the contact with the vadose zone. 7) Gas venting at the surface and associated processes of ground deformation leading to geomorphological feature formation.

reduction is kinetically limited and requires the presence of mineral catalysts. Gases migrate towards the surface as dissolved species in groundwater up to the vadose zone where they exsolve and can vent in a variety of geomorphological features. The proposed zone rich in reduced components above gold ore deposit recalls the "reduced column" model proposed by Hamilton (1998) for gold deposit alteration (see also Cameron et al. (2004) and Klusman (2009)). In this latter model, Fe-carbonate alteration was not proposed but Fe^{2+}-bearing mineral alteration was thought to impose a low oxygen fugacity at depth and in the overlying sediments. The proposed reduced aqueous species were HS^- and Fe^{2+}_{aq}. Difference in aqueous species migration in the reduced column compared to its surroundings is also proposed for explaining the anomalous element concentration "rabbit-ear" pattern measured in soils (Smee, 1984). High CO_2 and CH_4 concentration and low O_2 concentration anomalies in soil air are known as markers of concealed mineralization (McCarthy et al., 1986; Pauwels et al., 1999; Lovell, 2000; Zhang, 2000; Polito et al., 2002; Muntean and Taufen, 2011). These anomalies have been related to the release of gas during fluid inclusion breakdown, biological respiration and to the alteration of the carbonate gangue. This latter interpretation is consistent with the model proposed here.

5.4. Geomorphological feature formation in association with gas venting

In our search for geomorphological structure, special care was dedicated to the exclusion of regions where processes not related to gold deposits can lead to ground depression formation. However, we could not completely rule out the role played by other processes in the formation of some of the morphological features described here. First, 8 occurrences are located in karstic areas (Table 1). H_2 was measured in three of these localities (Zgonnik et al., 2015; Prinzhofer et al., 2019; Zgonnik, 2020). However, it is still unclear if the processes involved in H_2 formation are also responsible for ground depression for example by enhancing karst development and sinkhole formation. Observations in South Africa indicated that ground depressions can extend over larger areas than carbonate-rich units known to be involved in karst development. Dolomite occurs in the Gauteng, North West and Northern Cape provinces but not in the Free State province (Oosthuizen and Richardson, 2011). Interestingly, ground depressions were found in this latter province in a goldfield located south of the Witwatersrand basin near Welkom city (Supplementary Figure S1). This suggests that the presence of a karst network is not the only reason for ground depression formation in South Africa.

The square shape of some depressions observed in six localities is intriguing (Figure 2 H; Table 1). Natural lakes with rectangular shapes have been described in glaciolacustrine and alluvial sediments in Yukon (Canada; Old Crow Flats; (Roy-Léveillée and Burn, 2010)) and in the Beni basin (northeastern Bolivia; (Plafker, 1964)), respectively. Their origin is still unclear but their occurrence in sedimentary basins in both arctic and tropical latitudes indicates that their formation is controlled by climate-independent processes such as tectonics (faults in the basement) or wind/wave action (Lombardo and Veit, 2014). We cannot exclude that some of the ground depressions described here are related to human activities. However, several observations suggested a natural origin. First, square-shaped depressions were not only found in fields but also in forest area (Supplementary Figure 2 A). Then, the transition between depression-bearing and depression-free regions is sharp across field areas, which is not expected in similar fields (Supplementary Figure S2 B). Finally, large (> 50 m) semi-circular and small squared-shape depressions both occur at the same location for example in Western Australia (ON°27 and 28) and in Victoria (ON°30). One of the studied area with the largest human footprint is the San Joaquin valley in California. The ground depressions were only observed on the eastern part of the valley along the Sierra Nevada Foothills where orogenic gold deposits such as the Grass Valley District do occur (Taylor et al., 2021). Interestingly, small depressional wetlands, i.e. vernal pools, are known to occur in the same eastern part of the San Joaquin valley (Mooney and Zavaleta, 2016).

Karst development and human activity cannot explain all the observations made here, suggesting that other mechanisms related to the presence of orogenic gold deposits are involved in the development of ground depressions and self-organized spots of barren soil. S. Hamilton, who first proposed the reduced column model on which the model of Figure 6 is based (Hamilton, 1998), also studied geomorphological structures known as forest rings in boreal forests in

Ontario (Canada; Hamilton and Hattori (2008); Brauneder et al. (2016); von Gunten et al. (2018)). Forest rings are depressed circular features commonly exceeding 500 m in diameter with a low tree density. Anomalously high concentrations in CO_2 and in reduced species such as H_2S and CH_4, and low concentrations in O_2 were measured in their center. They were interpreted as the surficial expression of reduced feature alteration in the bedrock (Hamilton and Hattori, 2008). The region where they are found hosts numerous world-class gold deposits of the Abitibi Greenstone belt. For example, some forest rings described in Giroux et al. (2001) are located at less than 10 km from the Casa Berardi mine where ankerite precipitation is associated with gold mineralization (La Flèche and Camiré, 1996). All these observations and their interpretation suggest that forest rings belongs to the same type of structure as the ground depressions studied here, and could be formed as a result of Fe-carbonate dissolution at depth in orogenic gold deposits (Figure 6). Drilling revealed that mineral deposits do not directly underlain forest rings (Brauneder et al., 2016). This suggests that reduced species are also transported horizontally before reaching the surface, as it is expected during fluid flow in aquifers (Figure 6). Majeed (2020) did not detect H_2 in the soil of forest rings but their instrument had a detection limit of 500 ppm, which is above the H_2 concentration measured in most ground depressions (Zgonnik et al., 2015; Prinzhofer et al., 2018, 2019; Frery et al., 2021).

The model proposed above has several implications for geomorphological feature formation at the surface. First, the presence of H_2 in soil strongly modifies the ecosystem and can thus be involved in the loss of vegetation and the drastic decrease of the microbial biomass content in the soil (Sukhanova et al., 2013). Actually, Myagkiy et al. (2020a) showed that the presence of H_2-bearing gas can change the soil microbiota within a couple of months. Naudé et al. (2011) proposed a geochemical origin for fairy circles based on the extraction of reduced gases (carbon monoxide and hydrocarbons; H_2 was not measured) from the soil of fairy circles in the Namib desert (Namibia). Hydrocarbon microseepages were considered to induce plant stress limiting vegetation development (Naudé et al., 2011).

Secondly, siderite incongruent dissolution into magnetite and dissolved gases induces a solid volume decrease of 50 %. This favors ground collapse and sinkhole formation through processes similar to those known in karst regions. Due to proximity of the reacting basement from the surface, volume change-induced sinkhole formation is expected to be more efficient in shallow sedimentary basins containing low strength materials. The impact of volume decrease on surface deformation in sedimentary basins is well documented on the seafloor. In this context, volume decrease originates from porewater expulsion and diagenesis, and is also associated with fluid (and in particular gas) migration (Harrington, 1985; Cartwright, 2011). Interestingly, the geomorphological structures observed on the seafloor share numerous similarities with the structures described here (Ma et al., 2021). Circular depressions known as pockmarks are the most common features. Their size ranges from several kilometers to several meters in diameter (Lundsten et al., 2019). Pockmarks of various sizes can occur in the same location, as observed here for < 20 m wide white spots coexisting with hundreds of meters wide ground depressions. Pockmark fields are not randomly organized with a main property being the small number of neighbors at small distance (Hammer, 2009; Cartwright et al., 2011; Mazzini et al., 2017). To compare distribution patterns with the same tools, we used the pockmark distribution at Big Sur, Troll and Rosetta provided in Hammer (2009) and Cartwright et al. (2011) to compute the previously undetermined pair-correlation function (Table 2). Big Sur and Troll pockmark fields have mean nearest-neighbor distances of several hundreds of meters and display no clear spatial pattern apart from neighbor avoidance. For the Rosetta pockmark field, the mean nearest-neighbor distance is one order of magnitude smaller, and $g(r)$ reaches a high maximum value at this distance indicating self-organization similar to the one observed on land for fairy circles. Small mean nearest-neighbor distance may be a key factor allowing for self-organization in such structures by reducing the probability for the occurrence of heterogeneities at the surface or in the underlying basin/regolith. Jürgens et al. (2021) noted the same relationship in their point pattern analysis of fairy circles in Angola with small g_{max} values for large mean nearest-neighbor distance. Comet-shaped and elliptical depressions are also described on the seafloor (Chen et al., 2015, 2020) and formed by a combination of gas venting generating pockmarks and surface properties such as bottom current direction or slope leading to the comet shape (Berton and Vesely, 2018). The comet-shaped white spots observed here in Madagascar, Tanzania, Zimbabwe and Burkina Faso occur on the slope of small hills with circular white spots at the top of the hill. The tail of the comet-shaped features is oriented downslope, which is consistent with the model proposed by Chen et al. (2020) for similar structures on the seafloor in association with gas venting. Moreover, elliptical pockmarks on the seafloor can have their main axis progressively rotating with distance (Hillman et al., 2015), leading to patterns similar to the "peacock feather-like" appearance described here (Figure 3 D). Finally, polygonal fault systems, formed as a result of contraction-driven shear failure, are commonly found in the vicinity of pockmarks on the seafloor (Cartwright, 2011; Ma et al., 2021). They lead to the formation of geometric patterns at different elevations with the idealized polygonal geometry being the hexagonal pattern (Cartwright, 2011). We observed here polygonal depressions with square shapes near gold deposits. Pockmarks and polygonal faults are also found near gold provinces for example in the Bass Strait between Victoria and Tasmania (Niyazi et al., 2021), near the Shandong Peninsula (Liu et al., 2019; Tang et al., 2021) and near the Otago Schist in New Zealand (Hoffmann et al., 2019). Their origin is not clearly established and could be constrained with measurement of H_2 concentration on the seafloor.

Dissolved CO_2 formed during siderite dissolution turns into bicarbonate ions (HCO_3^-) at low temperature (Supplementary file F2). High carbonate content in groundwater may be involved in calcite ($CaCO_3$) precipitation in the vadose zone, leading to hardened layers formation in soils (calcrete) (Alonso-Zarza and Wright, 2010). High gold contents are described in calcretes which are actually used for gold exploration (Lintern, 2015), confirming the potential link between such formations and orogenic gold deposit alteration. Even though the exact mechanism of calcrete formation near gold deposits remains unclear, our results indicate that Fe-carbonate dissolution at depth can generate CO_2 exhalation. This could trigger calcite-promoted soil cementation and induration in the vadose zone. Some ground depressions observed here in Spain, Western Australia, Victoria and California have whitish elevated margins perhaps related to calcrete formation. The high density of circular white spots (including some fairy circles) in Australia, Burkina Faso, Madagascar, Mali, Tanzania, Myanmar and Zimbabwe could also be related to carbonate precipitation in soils associated with abiotic CO_2 emission. Cramer et al. (2017) measured two times higher CO_2 efflux in soil at the border of fairy circles compared to their center and to the matrix in the interspaces. Moore and Picker (1991) and Potts et al. (2009) have shown that mima mounds (heuweltjies), thought to be the southern equivalent of fairy circles in western South Africa (Van Rooyen et al., 2004), are spatially correlated with the presence of lenses of calcrete. Mima mound formation can host termite nests (Potts et al., 2009). Carbonates are commonly found in termite mounds where they are formed by abiotic processes (Mujinya et al., 2011; Francis and Poch, 2019). Interestingly, termite mounds contain systematically higher Au contents than their surrounding matrix. They are thus preferred soil sampling medium for gold exploration in regions covered with a thick regolith such as in Australia (Petts et al., 2009; Stewart et al., 2012), Ethiopia (Kebede, 2004), Ghana (Arhin and Nude, 2010), and Niger (Gleeson and Poulin, 1989). Boadi (2019) showed that termite mounds in southwest Ghana are aligned along a NE-SW trend similar to the regional structures of the Birimian Greenstone Belt, suggesting that termite mound formation is controlled by tectonics or the composition of rocks in the basement. Stewart and Anand (2014) showed that Au is associated with a higher calcite content in the termite mounds. They also reported high Au content in other insect nests such as ant nests. This suggests that high Au concentration in termite mounds is rather associated with the formation of calcrete rather than to termite activity. Metal transfer in regolith can occur through a variety of processes including groundwater flow, capillary migration, biological transfer and gaseous transport (Anand et al., 2016). This latter process is particularly interesting regarding the model developed here involving gas formation during alteration. Using a funnel system equipped with a thin membrane, Kristiansson and Malmqvist (1987) first observed metal transport associated with gas bubbles (called geogas) in soils above concealed deposits. Since then, metals carried by gases including CO_2 have been observed in the cover of numerous ore deposits (Wang et al., 1997; Pauwels et al., 1999; Gao et al., 2011; Noble et al., 2013; Lu et al., 2019). Metal transport with gas was reproduced in the laboratory (Cao et al., 2010) and the transported nanoparticles have been imaged with transmission electron microscopy (Wei et al., 2013; Han et al., 2020).

The soil physical properties of fairy circles and termite mounds contrast with those of the matrix surrounding the fairy circles. In Namibia, infiltration rate and hydraulic conductivity in fairy circles are significantly higher than in the matrix (Ravi et al., 2017; Cramer et al., 2017). Ravi et al. (2017) measured a decrease in soil granulometry and an improved sorting of the soil particles (small deviation from the mean particle size) at the edges of the fairy circles. In Australia, the highest water content in soil was measured at the edges of the fairy circles due to the presence of a clay crust in the center (Getzin et al., 2021a). Mujinya et al. (2013) also measured enrichment in 2:1 layer silicates and mica in termite mounds. This recalls the shaly deposits described in larger ground depressions (Myagkiy et al., 2020b), where the highest H_2 concentrations are measured at the border of the structure due to low permeability in the center (Prinzhofer et al., 2019). Moore and Picker (1991) reported a strong difference in soil granulometry in termite mounds with sandy-to-silty soils in the mounds, and gravels in the matrix. Interestingly, similar grain size distribution and sorting are observed in self-organized stone sorted circles observed in Arctic permafrost regions (Hallet, 2013). These last geomorphological structures are associated with the propagation of a freezing front inducing soil convection (frost heaving). Carbonate dissolution and precipitation in calcrete during wet and dry seasons, respectively, could play a similar role in fairy circle and termite mound formation in semi-arid conditions. Consistently, carbonate microtexture in termite mounds indicates successive episodes of dissolution and precipitation (Mujinya et al., 2011; Francis and Poch, 2019).

The above evidence converges on a link between Fe-carbonate dissolution, gold mobility, gas exhalation, calcrete formation in semi-arid terrains, and geomorphological feature formation at the surface. However, the exact mechanisms linking these processes are still poorly understood and will require further investigation. In particular, attention should be devoted to understanding the couplings between the geosphere and the biosphere in the context of gas seepage at the surface.

5.5. Generalization to other formations unrelated to gold deposits

Fe-carbonates in the Earth's crust are not restricted to orogenic gold deposits. They are abundant in other ore deposits, iron formations, carbonate-rich magmatic rocks (carbonatites) and sedimentary rocks. Those formations are thus expected to produce H_2 through alteration processes similar to the ones proposed here. Ground depressions and high density of small barren spots can also be found in these formations. For example, ground depressions were found here in the Iberian pyrite belt (Figure 7 A). The Iberian pyrite belt is composed of massive sulfide deposits formed during hydrothermal circulation on the seafloor. Carbonation associated with hydrothermalism is described in some units in the Iberian pyrite belt. Ankerite can form ~ 10 % of the rock (Tornos et al., 1997). Additionally, one of the place extensively studied for termite mound organization and composition is the Lubumbashi area (DR Congo; Mujinya et al. (2011, 2013, 2014)). High Cu and Co concentrations are measured in the mounds relative to the surrounding matrix (Mpinda et al., 2022). This area is part of the Central African Copperbelt where Schmandt et al. (2013) observed ankerite precipitation associated with copper deposit formation.

A high density of circular white spots is found on the border of the Chilwa Lake in the Chilwa Alkaline Province (Figure 7 B). Sideritic and ankeritic car-

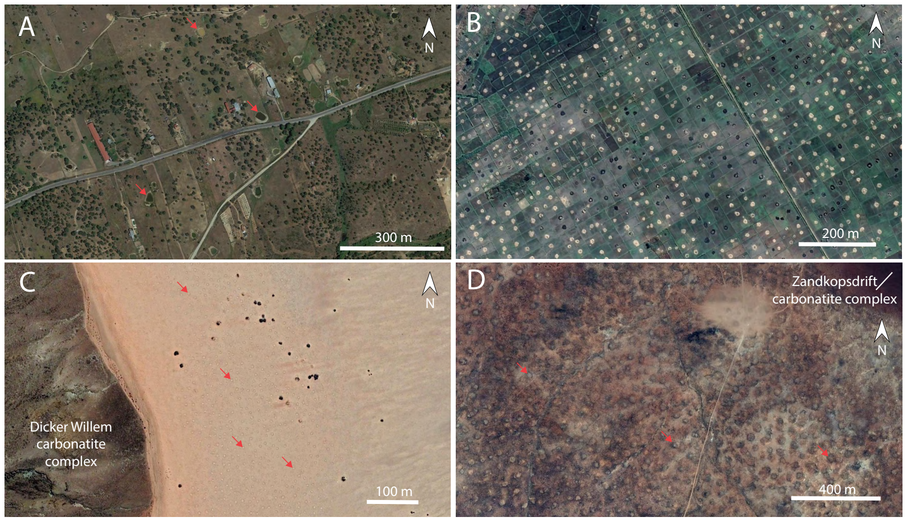

Figure 7: Geomorphological features associated with formations other than orogenic gold deposits. A: ground depressions (some are indicated with red arrows) located in the Iberian Pyrite belt, 20 km to the west of the Telmo mine (37°47'14"N, 7°12'58"W). B: high density of white circular spots on the shore of the Chilwa Lake (Malawi), part of the Chilwa Alkaline Province (15°8'34"S, 35°32'42"E). C: spatial relationship between the Dicker Willem carbonatite complex and fairy circles (26°28'3"S, 16°1'21"E; Namibia). The red arrows point towards fairy circles only present at the margin of the carbonatite complex. D: spatial relationship between the Zandkopsdrift carbonatite complex and mima mounds ("heuweltjies") in South Africa (30°51'56"S, 17°57'49"E).

bonatites are described on the Chilwa Island (Dowman et al., 2017). Similar white spots are found near the carbonatites of the East African Rift in Uganda (west of Sukulu carbonatite, see .kmz file). Namibia, western South Africa and Angola, where fairy circles and mima mounds ("heuweltjies") have been previously described, contain one of the highest density of carbonatites in the world, in which Fe-carbonates can be dominant (Drüppel et al., 2005; Woolley and Kjarsgaard, 2008). The close spatial relationship between carbonatites and geomorphological features is striking in some areas. For example, fairy circles concentrate at the border of the Dicker Willem carbonatite complex (Figure 7 C). In this latter locality, carbonates are calcite and minor Fe-bearing dolomite (Reid and Cooper, 1992). The description of iron staining at calcite surface is compatible with late oxidation of Fe-carbonate. In South Africa, the spatial link between carbonatites and mima mounds also clearly appears on satellite images for example near the Zankopsdrift carbonatite complex (Figure 7 D) containing Fe-carbonates (Ogungbuyi et al., 2022). Similar mima mounds occur in the Bahia State in Brazil where they are called murundus (de Souza and Delabie, 2016). We found murundus in the vicinity of carbonatite complexes for example at Angico dos Dias. Carbonatites in Brazil, Angola, Namibia and South Africa are part of the same Paran-Angola-Namibia magmatic province. We also determined the pair-correlation function for geomorphological feature patterns found in the vicinity of carbonatites in Brazil, Malawi, Namibia and South Africa (Table 2 and Supplementary Figure S3). The lowest g_{max} values were computed in Malawi and Namibia whereas high values above 1.3 were obtained in Brazil and South Africa (murundus and heuweltjie; Moore and Picker (1991); de Souza and Delabie (2016)). For these two latter occurrences, $g(r)$ displays a wave-like form with periodic deviation from the random-null model, indicating a high degree of spatial ordering (Supplementary Figure S3). This suggests that self-organization is not specific to fairy circles, and may rather require homogeneous subsurface environmental properties. The spatial link between fairy circles, mima mounds and carbonatites again suggests that the main process behind potentially self-organized geomorphological feature formation in the Paran-Angola-Namibia magmatic province is related to Fe-carbonate dissolution.

Microtextural observations of siderite replacement by magnetite in carbonatites from southwest Greenland have been interpreted as evidence for secondary hydrothermal alteration along fluid pathways (Ranta et al., 2018). In addition, magnetite only occurs together with sub-spherical grains of carbonaceous matter in ankeritic carbonatite from Somalia, suggesting formation during siderite breakdown as proposed by Gellatly (1966). Doroshkevich et al. (2007) and Doroshkevich et al. (2010) described similar spatial correlation between magnetite and carbonaceous matter in siderite carbonatites from Russia and India. However, carbonaceous matter formation was attributed to magmatic processes rather than to secondary alteration. Based on the thermodynamic calculations provided in the supplementary materials (Supplementary File F2), siderite dissolution could also take place during hydrothermal alteration of carbonatites at temperature below 200°C.

The fairy circles in Western Australia are observed 20 km east of the city of Newman (Getzin et al., 2019). They are hosted in geological formations, which are part of the Hamersley group outcropping in the southern margin of the Pilbara craton. In this region, some of the thickest banded iron formations in the world are observed. They contain numerous Fe-carbonates in which Rasmussen and Muhling (2018) described petrological evidence for secondary alteration with magnetite, carbonaceous matter and hydrogen production. The Mount Whaleback iron deposit is located at $\sim$ 25 km to the east of the fairy circles. Shales predominantly containing dolomite and ankerite are found below this deposit (Webb et al., 2006). We also observed other geomorphological features in the Hamersley province recalling fairy circles at $\sim$ 50 km to the north of the discovery of Getzin et al. (2016) (see kmz file for exact location). This suggests that fairy circles are relatively common near banded iron formation in Australia.

5.6. Implications for H_2 and gold exploration and global H_2 production

The model proposed here suggests that H_2 measurement and geomorphological feature mapping can be used as new tools for orogenic gold deposit exploration, especially in regolith-dominated terranes. These tools are relatively simple to use, both onshore and offshore. For example, in the course of this study, we identified several geomorphological features possibly indicating the

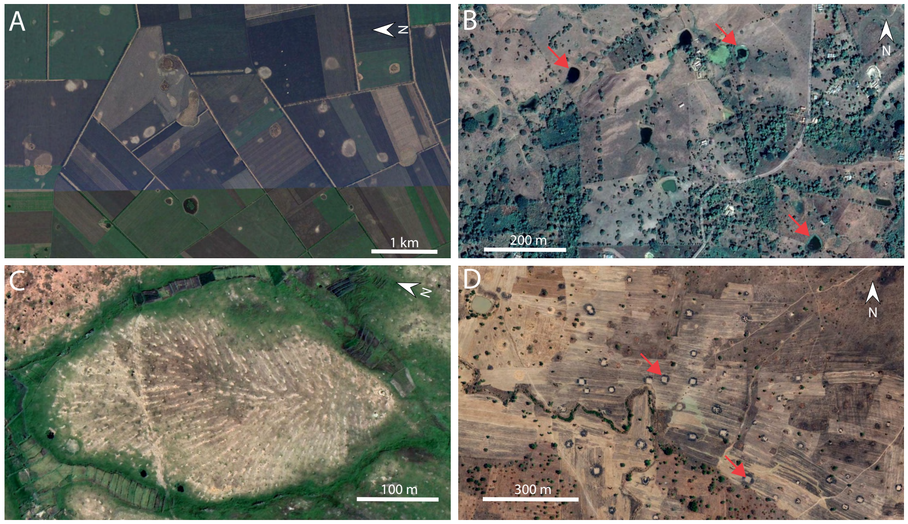

Figure 8: Geomorphological features possibly indicating the presence of Fe-carbonates and associated orogenic gold deposits. A: Barren ground depressions located in the south of Voronezh (Russia; 51°26'58"N, 39°24'37"E). This region is part of a Greenstone complex including several Greenstone belts, some of them hosting gold deposits at more than 100 km to the southwest of Voronezh (ON°26; de Boorder et al. (2006)). B: Ground depressions in the Sinu-San Jacinto basin (Colombia; 9°9'28"N, 75°59'50"W). The basin probably covers rocks in the structural continuity of the Setentrional Andes of Colombia outcropping in the South and hosting gold deposits (ON°11 and 12; Tassinari et al. (2008)). C: Comet-shaped barren white spots grouped into a "peacock feather-like" appearance in Madagascar at more than 80 km to the south-southwest of the Ambia gold deposit (23°14'17"S, 45°56'5"E). The tails of the comet-shaped spots are oriented downslope. Ground depressions and white spots are also found near this deposit (ON°2; Rambeloson (1999)). D: Squared-shape depressions at 30 km to the north of the Tamale city in Ghana (9°39'39"N 0°55'46"O). Such features are common in the Volta basin overlying the greenstone belts of the Man-Leo shield, which is one of the world's largest gold province.

presence of gold deposits in Russia, Madagascar, Colombia and Ghana (Figure 8). These features occur in sedimentary basins at more than 80 km of known deposits or are found in geological units where gold has not yet been described to our knowledge. However, one should keep in mind that geomorphology should be combined with geological, geochemical and hydrological information for exploration. As shown above, several formations can indeed host Fe-carbonates, geomorphological features can have multiple origins, and it is not excluded that groundwater horizontally migrates over significant distances before reaching the vadose zone where gases are released. Moreover, the model proposed here and its generalization to other formations containing Fe-carbonates significantly increases the number of geological units which can be targeted for H_2 exploration. We indeed showed that, in crustal basement, not only Precambrian rocks but also Phanerozoic rocks should produce H_2 during alteration under sedimentary basins. We hope it will initiate gas measurement campaigns onshore and offshore to confirm the presence of H_2 and CO_2 production in association with Fe-carbonate-bearing formations. These formations are common in crustal rocks and have a high hydrogen production potential even at low temperature. However, they are restricted in volume.

Fe-carbonates in orogenic gold deposits only occur in and around metamorphic veins at a concentration of less than 30 wt.% (Eilu and Groves, 2001; Stromberg et al., 2018). The maximum mass of orogenic gold deposits can be estimated to 218 billions of tons by using a minimum grade of 1g/ton and a total of 218 000 tons of discovered gold to date (Butt and Hough, 2009; U.S. Geological Survey, 2022). Combining these numbers gives a maximum of 65 billions of tons of Fe-carbonates in orogenic gold deposits worldwide. Assuming that all Fe-carbonates are siderite ($FeCO_3$) and that H_2 is not consumed by carbon reduction nor sulfidation, we can use reaction 1 to estimate a global production of H_2 by Fe-carbonate dissolution in orogenic gold deposits of $\sim 2.10^{14}$ moles of H_2. The same type of calculation can be performed for iron formations. The maximum estimates of global iron ore resource are of 485 Gt (Mohr et al., 2015). Assuming that 10 % of this iron is hosted in siderite, a maximum estimate of the amount of siderite in iron formations is of 100 Gt, corresponding to a global H_2 production of 3.10^{14} moles of H_2 according to reaction 1. H_2 production potential can also be provided for carbonatites by estimating a global mass of carbonatites at the surface of $5.27.10^{11}$ tons with the total number of occurrences in the world and the maximum tonnage provided in Woolley and Kjarsgaard (2008) and Simandl and Paradis (2018), respectively. Using an average concentration in FeO of 4 wt.% in carbonatites (Gold, 1963) and a Fe:H_2 ratio of 3:1 as per reaction 1, the global production potential of carbonatites is estimated to $\sim 1.10^{14}$ moles of H_2.

Even when combining the above maximum values, the global H_2 production by Fe-carbonate reaction of 6.10^{14} moles of H_2 is 5 orders of magnitude smaller than the minimum previous estimates considering iron silicates for H_2 production by hydration in Precambrian rocks (4.10^{19} moles for production to depth of 1 km; Sherwood Lollar et al. (2014)). As shown above, the H_2 measurements used in this latter study were mainly acquired in gold mines or near gold deposits. There is thus a potential sampling bias and measurements in Fe-carbonate-free formations is required to better constrain global H_2 production in crustal rocks. For comparison with H_2 production during alteration on the seafloor, global H_2 production potentials are generally converted into flux by using rock age (Sherwood Lollar et al., 2014). As discussed above, formations containing Fe-carbonates of all ages exist. We therefore used here the mean age of the continental crust (2 Ga; Taylor and McLennan (1995)) to estimate a global H_2 flux of 3.10^5 mol/yr as a first approximation. This latter value is approximately 6 orders of magnitude smaller than H_2 flux estimates for ocean crust alteration (Bach and Edwards, 2003) and serpentinization at slow-spreading mid-ocean ridges (Cannat et al., 2010). Whereas Fe-carbonate dissolution seems to control the formation of geomorphological features, this geochemical process may be represent a marginal contribution to the overall H_2 production budget in the Earth's crust.

6. Conclusions

The main conclusions of this study on Fe-carbonate alteration in orogenic gold deposits are best summarized with the following points:

- In crustal basement, most previously published data of high H_2 concentrations in gas, groundwater and fluid inclusions were acquired in gold mines or near gold deposits. This concerned 34 localities.

- The spatial link between orogenic gold deposits and H_2 production is supported by the mapping of geomorphological features in sedimentary basins overlying crustal basements, provided that these geomorphological features are reliable markers of H_2 emission.

- By mapping thousands of these morphological structures, two types of barren geomorphological features were observed in 32 localities over 20 countries: generally semi-circular ground depressions ranging in size from several hundreds of meters to several tens of meters, and high density of circular white spots less than 20 m wide. These white spots have a tail in the steep terrains, which gives a comet shape. The barren spots observed in the Yilgarn craton (Australia) and Mali are probably fairy circles, providing new occurrences for such features which have only been described in a single locality outside Namibia, South Africa and Angola. All these geomorphological features recall those found in offshore sedimentary basins where gas is venting. Moreover, they were observed in geological formations of all ages with a variety of composition including ultramafic/mafic rocks, iron formations, and sedimentary rocks. The common denominator of the occurrence of these geomorphological features is the presence of orogenic gold deposits at a distance < 100 km. This suggests a relationship between orogenic gold deposits, H_2 production and geomorphological feature formation. The presence of Fe-carbonates (i.e. siderite, ankerite) in gold deposits plays a key role on abiotic H_2 production. H_2 and CO_2 are rapidly produced during Fe-carbonate interaction with water at low temperature (T < 200°C). Reduced carbon species (CH_4, light hydrocarbons and carbonaceous matter) can be formed by further reaction between the gaseous products of the reaction. However, this latter reaction is kinetically limited at low temperature and requires mineral catalysts. Fe-carbonate reaction with pyrite to form pyrrhotite also reduces the H_2 yield in orogenic gold deposits. Significant water to rock ratio (100 to 10000) is required for complete reaction, suggesting that the residence time of water in deep aquifer controls the H_2 yield.

- We combined the above results to propose a new model of H_2 production during low-temperature orogenic gold deposit alteration. The model considers fluid flow in sedimentary basin leading to Fe-carbonate dissolution in the underlying orogenic gold deposits. Produced gases then migrate towards the surface first as dissolved species and then as free gas. Gas venting generates a variety of geomorphological features at the surface. The exact mechanisms leading to such geomorphological structure formation have not yet been elucidated but involve interplays between hydrosphere, geosphere and biosphere. Probably important processes include volume decrease during Fe-carbonate dissolution, calcrete formation associated with CO_2 venting, vegetation death due to the presence of reduced gases, and particle sorting due to successive episodes of calcrete dissolution/precipitation.

- Whereas ground depressions have been proposed for natural H_2 exploration, they might also be used together with small white spots for orogenic gold deposit exploration with satellite images. Based on geomorphological feature observation, we proposed 35 and 4 new localities for H_2 and gold exploration, respectively.

- Our geochemical model also applies to iron formations and carbonatites, known to also contain significant amounts of Fe-carbonates. Geomorphological features believed to be associated with H_2 gas exhalation were also observed near these formations, supporting Fe-carbonate dissolution as a general mechanism of H_2 production in crustal basement.

- The H_2 production potential of Fe-carbonate alteration is at least 5 orders of magnitude smaller than estimates for continental crusts based on all available ferrous iron. Although the contribution of Fe-carbonate to natural H_2 production worldwide is expected to be small, it remains of paramount importance for the formation of the geomorphological features described here.

The observations performed here and the proposed model encompass a large range of geological formations. However, Fe-carbonates occurring in sedimentary rocks (excluding iron formations) were not considered. They may also contribute to H_2 production and impact the estimate of global H_2 production.

References

Abrajano, T., Sturchio, N., Kennedy, B., Lyon, G., Muehlenbachs, K., Bohlke, J., 1990. Geochemistry of reduced gas related to serpentinization of the Zambales ophiolite, Philippines. Applied Geochemistry 5 (5-6), 625–630.

Acar, C., Dincer, I., 2020. The potential role of hydrogen as a sustainable transportation fuel to combat global warming. International Journal of Hydrogen Energy 45 (5), 3396–3406.

Adomako-Ansah, K., Mizuta, T., Ishiyama, D., Hammond, N. Q., 2017. Nature of ore-forming fluid and formation conditions of BIF-hosted gold mineralization in the Archean Amalia Greenstone Belt, South Africa: Constraints from fluid inclusion and stable isotope studies. Ore Geology Reviews 89, 609–626.

Alarifi, S. S., Kellogg, J. N., Ibrahim, E., 2021. Geophysical study of gold mineralized zones in the Carolina terrane of South Carolina. Economic Geology 116 (6), 1309–1327.

Alonso-Zarza, A. M., Wright, V. P., 2010. Chapter 5 Calcretes. Vol. 61. Elsevier, pp. 225–267.

Anand, R. R., Aspandiar, M. F., Noble, R. R., 2016. A review of metal transfer mechanisms through transported cover with emphasis on the vadose zone within the Australian regolith. Ore Geology Reviews 73, 394–416.

Arce-Burgoa, O. R., Goldfarb, R. J., 2009. Metallogeny of Bolivia. SEG Discovery (79), 1–15.

Arhin, E., Nude, P. M., 2010. Use of termitaria in surficial geochemical surveys: evidence for ¿125-μm size fractions as the appropriate media for gold exploration in northern Ghana. Geochemistry: Exploration, Environment, Analysis 10 (4), 401–406.

Arrouvel, C., Prinzhofer, A., 2021. Genesis of natural hydrogen: New insights from thermodynamic simulations. International Journal of Hydrogen Energy 46 (36), 18780–18794.

Artemieva, I. M., 2006. Global 1 1 thermal model TC1 for the continental lithosphere: Implications for lithosphere secular evolution. Tectonophysics 416 (1-2), 245–277.

Ayarza, P., Villalaín, J. J., Martínez Catalán, J. R., Álvarez Lobato, F., Durán Oreja, M., Calvín, P., Recio, C., Suárez Barrios, M., Gómez Martín, E., 2021. Characterizing the Source of the Eastern Galicia Magnetic Anomaly (NW Spain): The Role of Extension in the Origin of Magnetization at the Central Iberian Arc. Tectonics 40 (3), e2020TC006120.

Bach, W., Edwards, K. J., 2003. Iron and sulfide oxidation within the basaltic ocean crust: Implications for chemolithoautotrophic microbial biomass production. Geochimica et Cosmochimica Acta 67 (20), 3871–3887.

Baddeley, A., Turner, R., 2005. spatstat : An R Package for Analyzing Spatial Point Patterns. Journal of Statistical Software 12 (6), 1–42.

Bateman, R., Hagemann, S., 2004. Gold mineralisation throughout about 45 Ma of Archaean orogenesis: Protracted flux of gold in the Golden Mile, Yilgarn craton, Western Australia. Mineralium Deposita 39 (5-6), 536–559.

Bekker, A., Slack, J. F., Planavsky, N., Krapež, B., Hofmann, A., Konhauser, K. O., Rouxel, O. J., 2010. Iron formation: The sedimentary product of a complex interplay among mantle, tectonic, oceanic, and biospheric processes. Economic Geology 105 (3), 467–508.

Belogub, E. V., Melekestseva, I. Y., Novoselov, K. A., Zabotina, M. V., Tret'yakov, G. A., Zaykov, V. V., Yuminov, A. M., 2017. Listvenite-related gold deposits of the South Urals (Russia): A review. Ore Geology Reviews 85, 247–270.

Berezovsky, A., Pieczonka, J., Piestrzynski, A., 2021. Silver-gold and polymetallic mineralization in the banded iron formations deposit in Kryvyi Rih, Ukraine. Precambrian Research 363, 106326.

Berndt, M. E., Allen, D. E., Seyfried, W. E., 1996. Reduction of CO2 during serpentinization of olivine at 300 degrees C and 500 bar. Geology 24 (4), 351–354.

Berton, F., Vesely, F. F., 2018. Origin of buried, bottom current-related comet marks and associated submarine bedforms from a Paleogene continental margin, southeastern Brazil. Marine Geology 395, 347–362.

Black, J. R., Carroll, S. A., Haese, R. R., 2015. Rates of mineral dissolution under CO2 storage conditions. Chemical Geology 399, 134–144.

Blundell, C. C., Armit, R., Ailleres, L., Micklethwaite, S., Martin, A., Betts, P., 2019. Interpreting geology from geophysics in poly-deformed and mineralised terranes; the Otago Schist and the Hyde-Macraes Shear Zone. New Zealand Journal of Geology and Geophysics 62 (4), 550–572.

Boadi, S., 2019. Using Spatial Distribution of Termite Mounds To Support Subsurface Geological Imaging In A Complex Regolith Terrain of Sefwi-Bibiani Gold Belt, SW Ghana. International Journal of Geoinformatics and Geological Science 6 (3), 40–47.

Bohlke, J. K., Kistler, R. W., 1986. Rb-Sr, K-Ar, and stable isotope evidence for the ages and sources of fluid components of gold-bearing quartz veins in the northern Sierra Nevada foothills metamorphic belt, California. Economic Geology 81 (2), 296–322.

Boreham, C. J., Sohn, J. H., Cox, N., Williams, J., Hong, Z., Kendrick, M. A., 2021. Hydrogen and hydrocarbons associated with the Neoarchean Frog's Leg Gold Camp, Yilgarn Craton, Western Australia. Chemical Geology 575, 120098.

Boyle, R. W., 1955. The geochemistry and origin of the gold bearing quartz veins and lenses of the yellow-knife greenstone belt. Economic Geology 50 (1), 51–66.

Brauneder, K., Hamilton, S. M., Hattori, K., 2016. Geochemical processes in the formation of forest rings': Examples of reduced chimney formation in the absence of mineral deposits. Geochemistry: Exploration, Environment, Analysis 16 (1), 85–99.

Brunet, F., 2019. Hydrothermal Production of H2 and Magnetite From Steel Slags: A Geo-Inspired Approach Based on Olivine Serpentinization. Frontiers in Earth Science 7, 17.

Butt, C. R., Hough, R. M., 2009. Why gold is valuable. Elements 5 (5), 277–280.

Cameron, E. M., Hamilton, S. M., Leybourne, M. I., Hall, G. E., McClenaghan, M. B., 2004. Finding deeply buried deposits using geochemistry. Geochemistry: Exploration, Environment, Analysis 4 (1), 7–32.

Cannat, M., Fontaine, F., Escartín, J., 2010. Serpentinization and associated hydrogen and methane fluxes at slow spreading ridges. American Geophysical Union, pp. 241–264.

Cao, J. J., Hu, X. Y., Jiang, Z. T., Li, H. W., Zou, X. Z., 2010. Simulation of adsorption of gold nanoparticles carried by gas ascending from the Earth's interior in alluvial cover of the middle-lower reaches of the Yangtze River. Geofluids 10 (3), 438–446.

Cartwright, A., Moss, J., Cartwright, J., 2011. New statistical methods for investigating submarine pockmarks. Computers and Geosciences 37 (10), 1595–1601.

Cartwright, J., 2011. Diagenetically induced shear failure of fine-grained sediments and the development of polygonal fault systems. Marine and Petroleum Geology 28 (9), 1593–1610.

Cerlienco, B. P., 2009. Geological setting and alteration characteristics of the Hillside mineralising system, Yorke Peninsula. Ph.D. thesis, University of Adelaide.

Charlou, J. L., Donval, J. P., Fouquet, Y., Jean-Baptiste, P., Holm, N., 2002. Geochemistry of high H2 and CH4 vent fluids issuing from ultramafic rocks at the Rainbow hydrothermal field (3614'N,MAR). Chemical Geology 191 (4), 345–359.

Chen, J., Song, H., Guan, Y., Yang, S., Pinheiro, L. M., Bai, Y., Liu, B., Geng, M., 2015. Morphologies, classification and genesis of pockmarks, mud volcanoes and associated fluid escape features in the northern Zhongjiannan Basin, South China Sea. Deep-Sea Research Part II: Topical Studies in Oceanography 122, 106–117.

Chen, T. T., Paull, C. K., Liu, C. S., Klaucke, I., Hsu, H. H., Su, C. C., Gwiazda, R., Caress, D. W., 2020. Discovery of numerous pingos and comet-shaped depressions offshore southwestern Taiwan. Geo-Marine Letters 40 (4), 407–421.

Chi, J., Yu, H., 2018. Water electrolysis based on renewable energy for hydrogen production. Cuihua Xuebao/Chinese Journal of Catalysis 39 (3), 390–394.

Chinnasamy, S. S., Mishra, B., 2017. Genetic implications of fluid-deposited disordered graphite and methane-rich inclusions in the Jonnagiri granodiorite-hosted gold deposit, Eastern Dharwar Craton, India. Ore Geology Reviews 89, 587–593.

Christie, A. B., Brathwaite, R. L., 2003. Hydrothermal alteration in metasedimentary rock-hosted orogenic gold deposits, Reefton goldfield, South Island, New Zealand. Mineralium Deposita 38 (1), 87–107.

Conrad, R., 1996. Soil microorganisms as controllers of atmospheric trace gases (H2, CO, CH4, OCS, N2O, and NO). Microbiological Reviews 60 (4), 609–640.

Conrad, R., Seiler, W., 1980. Contribution of hydrogen production by biological nitrogen fixation to the global hydrogen budget. Journal of Geophysical Research 85 (C10), 5493–5498.

Cook, A. P., Meyer, C. F., Balt, K., 1999. Flammable gas emissions in South African gold and platinum mines. Review of incidents and accidents. Proceedings of the 8th US mine ventilation symposium, 105–109.

Cramer, M. D., Barger, N. N., Tschinkel, W. R., 2017. Edaphic properties enable facilitative and competitive interactions resulting in fairy circle formation. Ecography 40 (10), 1210–1220.

Craw, D., Upton, P., Yu, B. S., Horton, T., Chen, Y. G., 2010. Young orogenic gold mineralisation in active collisional mountains, Taiwan. Mineralium Deposita 45 (7), 631–646.

Cudby, J., Scott, J. M., Craw, D., Hesson, M., Rufaut, C., 2021. Surficial redistribution of gold and arsenic from the Rise and Shine Shear Zone, Otago, New Zealand. New Zealand Journal of Geology and Geophysics, 1–15.

de Boorder, H., Zeylmans van Emmichoven, M. J., Privalov, V. A., 2006. Distribution of Precambrian iron and gold deposits on the southwestern East European Platform reflected in underlying transcrustal structure and current river systems. Ore Geology Reviews 29 (3-4), 242–259.

de Souza, H. J., Delabie, J. H. C., 2016. Murundus' structures in the semi-arid region of Brazil: testing their geographical congruence with mound-building termites (Blattodea: Termitoidea: Termitidae). Annales de la Societe Entomologique de France 52 (6), 369–385.

Deville, E., Prinzhofer, A., 2016. The origin of N2-H2-CH4-rich natural gas seepages in ophiolitic context: A major and noble gases study of fluid seepages in New Caledonia. Chemical Geology 440, 139–147.

Dincer, I., Acar, C., 2014. Review and evaluation of hydrogen production methods for better sustainability. International Journal of Hydrogen Energy 40 (34), 11094–11111.

Doroshkevich, A. G., Ripp, G., Viladkar, S., 2010. Newania carbonatites, Western India: Example of mantle derived magnesium carbonatites. Mineralogy and Petrology 98 (1-2), 283–295.

Doroshkevich, A. G., Wall, F., Ripp, G. S., 2007. Magmatic graphite in dolomite carbonatite at Pogranichnoe, North Transbaikalia, Russia. Contributions to Mineralogy and Petrology 153 (3), 339–353.

Dowman, E., Wall, F., Treloar, P. J., Rankin, A. H., 2017. Rare-earth mobility as a result of multiple phases of fluid activity in fenite around the Chilwa Island Carbonatite, Malawi. Mineralogical Magazine 81 (6), 1367–1395.

Drennan, G. R., Boiron, M. C., Cathelineau, M., Robb, L. J., 1999. Characteristics of post-depositional fluids in the Witwatersrand Basin. Mineralogy and Petrology 66 (1-3), 83–109.

Drew, L. J., Berger, B. R., Kurbanov, N. K., 1996. Geology and structural evolution of the Muruntau gold deposit, Kyzylkum desert, Uzbekistan. Ore Geology Reviews 11 (4), 175–196.

Drüppel, K., Hoefs, J., Okrusch, M., 2005. Fenitizing processes induced by ferrocarbonatite magmatism at Swartbooisdrif, NW Namibia. Journal of Petrology 46 (2), 377–406.

Dubé, B., K., W., Malo, M., 2003. Gold mineralization within the Red Lake mine trend: Example from the Cochenour-Willans mine area, Red Lake, Ontario, with new key information from the Red Lake mine and potential analogy with the Timmins camp.

Dugdale, A. L., Wilson, C. J., Leader, L. D., Robinson, J. A., Dugdale, L. J., 2009. Carbonate spots: Understanding the relationship to gold mineralization in Central Victoria, southeastern Australia. Mineralium Deposita 44 (2), 205–219.

Eilu, P., 2015. Overview on Gold Deposits in Finland. In: Mineral Deposits of Finland. Elsevier, pp. 377–410.

Eilu, P., Groves, D. I., 2001. Primary alteration and geochemical dispersion haloes of Archaean orogenic gold deposits in the Yilgarn Craton: The pre-weathering scenario. Geochemistry: Exploration, Environment, Analysis 1 (3), 183–200.

Ershov, B. G., 2020. Natural radioactivity and formation of oxygen in Earth's atmosphere: Decay of radioactive 40K and radiolysis of ocean water. Precambrian Research 346, 105786.

Etiope, G., 2017. Abiotic Methane in Continental Serpentinization Sites: An Overview. Procedia Earth and Planetary Science 17, 9–12.

Etiope, G., Samardžić, N., Grassa, F., Hrvatović, H., Miošić, N., Skopljak, F., 2017. Methane and hydrogen in hyperalkaline groundwaters of the serpentinized Dinaride ophiolite belt, Bosnia and Herzegovina. Applied Geochemistry 84, 286–296.

Etiope, G., Sherwood Lollar, B., 2013. Abiotic methane on earth. Reviews of Geophysics 51 (2), 276–299.

Foley, N., Ayuso, R. A., Seal, R., 2001. Remnant colloform pyrite at the haile gold deposit, South Carolina: A textural key to genesis. Economic Geology 96 (4), 891–902.

Ford, A., Hagemann, S. G., Fogliata, A. S., Miller, J. M., Mol, A., Doyle, P. J., 2015. Porphyry, epithermal, and orogenic gold prospectivity of Argentina. Ore Geology Reviews 71, 655–672.

Francis, M. L., Poch, R. M., 2019. Calcite accumulation in a South African heuweltjie: Role of the termite Microhodotermes viator and oribatid mites. Journal of Arid Environments 170, 103981.

Frery, E., Langhi, L., Maison, M., Moretti, I., 2021. Natural hydrogen seeps identified in the North Perth Basin, Western Australia. International Journal of Hydrogen Energy 46 (61), 31158–31173.

Gaboury, D., 2013. Does gold in orogenic deposits come from pyrite in deeply buried carbon-rich sediments?: Insight from volatiles in fluid inclusions. Geology 41 (12), 1207–1210.

Gaboury, D., MacKenzie, D., Craw, D., 2021. Fluid volatile composition associated with orogenic gold mineralization, Otago Schist, New Zealand: Implications of H2 and C2H6 for fluid evolution and gold source. Ore Geology Reviews 133, 104086.

Gaboury, D., Nabil, H., Ennaciri, A., Maacha, L., 2020. Structural setting and fluid composition of gold mineralization along the central segment of the Keraf suture, Neoproterozoic Nubian Shield, Sudan: implications for the source of gold. International Geology Review 64 (1), 45–71.

Gao, Y., Wang, M., en Zhang, D., 2011. Application of 'metals-in-soil-gas' techniques to mineral exploration inexotic overburden. Geochemistry: Exploration, Environment, Analysis 11 (2), 63–70.

Gellatly, D. C., 1966. Graphite in natural and experimental carbonate systems. Mineralogical Magazine and Journal of the Mineralogical Society 35 (275), 963–970.

Getzin, S., Erickson, T. E., Yizhaq, H., Muñoz-Rojas, M., Huth, A., Wiegand, K., 2021a. Bridging ecology and physics: Australian fairy circles regenerate following model assumptions on ecohydrological feedbacks. Journal of Ecology 109 (1), 399–416.

Getzin, S., Wiegand, K., Wiegand, T., Yizhaq, H., von Hardenberg, J., Meron, E., 2015. Adopting a spatially explicit perspective to study the mysterious fairy circles of Namibia. Ecography 38 (1), 1–11.

Getzin, S., Yizhaq, H., Bell, B., Erickson, T. E., Postle, A. C., Katra, I., Tzuk, O., Zelnik, Y. R., Wiegand, K., Wiegand, T., Meron, E., Hastings, A., 2016. Discovery of fairy circles in Australia supports self-organization theory. Proceedings of the National Academy of Sciences of the United States of America 113 (13), 3551–3556.

Getzin, S., Yizhaq, H., Muñoz-Rojas, M., Wiegand, K., Erickson, T. E., 2019. A multi-scale study of Australian fairy circles using soil excavations and drone-based image analysis. Ecosphere 10 (2), e02620.

Getzin, S., Yizhaq, H., Tschinkel, W. R., 2021b. Definition of fairy circles and how they differ from other common vegetation gaps and plant rings. Journal of Vegetation Science 32 (6), e13092.

Geymond, U., Ramanaidou, E., Lévy, D., Ouaya, A., Moretti, I., 2022. Can Weathering of Banded Iron Formations Generate Natural Hydrogen? Evidence from Australia, Brazil and South Africa. Minerals 12 (2), 163.

Giroux, J. F., Bergeron, Y., Veillette, J. J., 2001. Dynamics and morphology of giant circular patterns of low tree density in black spruce stands in northern Quebec. Canadian Journal of Botany 79 (4), 420–428.

Gleeson, C. F., Poulin, R., 1989. Gold exploration in Niger using soils and termitaria. Journal of Geochemical Exploration 31 (3), 253–283.

Glover, P. E., Trump, E. C., Wateridge, L. E. D., 1964. Termitaria and Vegetation Patterns on the Loita Plains of Kenya. The Journal of Ecology 52 (2), 367.

Gold, D. P., 1963. Average chemical composition of carbonatites. Economic Geology 58 (6), 988–991.

Goldfarb, R. J., Groves, D. I., 2015. Orogenic gold: Common or evolving fluid and metal sources through time. Lithos 233, 2–26.

Goldfarb, R. J., Groves, D. I., Gardoll, S., 2001. Orogenic gold and geologic time: a global synthesis. Ore Geology Reviews 18 (1-2), 1–75.

Goldfarb, R. J., Taylor, R. D., Collins, G. S., Goryachev, N. A., Orlandini, O. F., 2014. Phanerozoic continental growth and gold metallogeny of Asia. Gondwana Research 25 (1), 48–102.

Goldscheider, N., Chen, Z., Auler, A. S., Bakalowicz, M., Broda, S., Drew, D., Hartmann, J., Jiang, G., Moosdorf, N., Stevanovic, Z., Veni, G., 2020. Global distribution of carbonate rocks and karst water resources. Hydrogeology Journal 28 (5), 1661–1677.

Gregory, S. P., Barnett, M. J., Field, L. P., Milodowski, A. E., 2019. Subsurface microbial hydrogen cycling: Natural occurrence and implications for industry. Microorganisms 7 (2), 53.

Grenthe, I., Stumm, W., Laaksuharju, M., Nilsson, A. C., Wikberg, P., 1992. Redox potentials and redox reactions in deep groundwater systems. Chemical Geology 98 (1-2), 131–150.

Halas, P., Dupuy, A., Franceschi, M., Bordmann, V., Fleury, J. M., Duclerc, D., 2021. Hydrogen gas in circular depressions in South Gironde, France: Flux, stock, or artefact? Applied Geochemistry 127, 104928.

Hallet, B., 2013. Stone circles: Form and soil kinematics. Philosophical Transactions of the Royal Society A: Mathematical, Physical and Engineering Sciences 371 (2004).

Hamilton, S. M., 1998. Electrochemical mass-transport in overburden: A new model to account for the formation of selective leach geochemical anomalies in glacial terrain. Journal of Geochemical Exploration 63 (3), 155–172.

Hamilton, S. M., Hattori, K. H., 2008. Spontaneous potential and redox responses over a forest ring. Geophysics 73 (3).

Hammer, 2009. Pattern formation by local amplification and lateral inhibition: Examples from biology and geology. European Physical Journal: Special Topics 178 (1), 5–12.

Hammond, N. Q., Moore, J. M., 2006. Archaean lode gold mineralisation in banded iron formation at the Kalahari Goldridge deposit, Kraaipan Greenstone Belt, South Africa. Mineralium Deposita 41 (5), 483–503.

Han, Z., Zhang, B., Wu, H., Liu, H., Qiao, Y., Zhang, S., 2020. Microscopic characterisation of metallic nanoparticles in ore rocks, fault gouge and geogas from the Shanggong gold deposit, China. Journal of Geochemical Exploration 217, 106562.

Harrington, P. K., 1985. Formation of pockmarks by pore-water escape. Geo-Marine Letters 5 (3), 193–197.

Hillman, J. I., Gorman, A. R., Pecher, I. A., 2015. Geostatistical analysis of seafloor depressions on the southeast margin of New Zealand's South Island - Investigating the impact of dynamic near seafloor processes on geomorphology. Marine Geology 360, 70–83.

Hoffmann, J. J., Gorman, A. R., Crutchley, G. J., 2019. Seismic evidence for repeated vertical fluid flow through polygonally faulted strata in the Canterbury Basin, New Zealand. Marine and Petroleum Geology 109, 317–329.

Horita, J., Berndt, M. E., 1999. Abiogenic methane formation and isotopic fractionation under hydrothermal conditions. Science 285 (5430), 1055–1057.

Hrstka, T., Dubessy, J., Zachariáš, J., 2011. Bicarbonate-rich fluid inclusions and hydrogen diffusion in quartz from the Libčice orogenic gold deposit, Bohemian Massif. Chemical Geology 281 (3-4), 317–332.

Hu, S., Evans, K., Craw, D., Rempel, K., Bourdet, J., Dick, J., Grice, K., 2015. Raman characterization of carbonaceous material in the Macraes orogenic gold deposit and metasedimentary host rocks, New Zealand. Ore Geology Reviews 70, 80–95.

Hu, S. Y., Evans, K., Craw, D., Rempel, K., Grice, K., 2017. Resolving the role of carbonaceous material in gold precipitation in metasediment-hosted orogenic gold deposits. Geology 45 (2), 167–170.

Jürgens, N., Gunter, F., Oldeland, J., Groengroeft, A., Henschel, J. R., Oncken, I., Picker, M. D., 2021. Largest on earth: Discovery of a new type of fairy circle in Angola supports a termite origin. Ecological Entomology 46 (4), 777–789.

Kalinin, A. A., Kazanov, O. V., Bezrukov, V. I., Prokofiev, V. Y., 2019. Gold prospects in the western segment of the Russian arctic: Regional metallogeny and distribution of mineralization. Minerals 9 (3), 137.

Kebede, F., 2004. Use of termite mounds in geochemical exploration in North Ethiopia. Journal of African Earth Sciences 40 (1-2), 101–103.

Kita, I., Matsuo, S., Wakita, H., 1982. H 2 generation by reaction between H 2 O and crushed rock: An experimental study on H 2 degassing from the active fault zone. Journal of Geophysical Research: Solid Earth 87 (B13), 10789–10795.

Klein, C., 2005. Some Precambrian banded iron-formations (BIFs) from around the world: Their age, geologic setting, mineralogy, metamorphism, geochemistry, and origin. American Mineralogist 90 (10), 1473–1499.

Klein, F., Tarnas, J. D., Bach, W., 2020. Abiotic sources of molecular hydrogen on earth. Elements 16 (1), 19–24.

Klein, T. L., Cunningham, C. G., Logan, M. A., Seal, R. R., 2007. The Russell gold deposit, Carolina Slate Belt, North Carolina. Economic Geology 102 (2), 239–256.

Klusman, R. W., 2009. Transport of ultratrace reduced gases and particulate, near-surface oxidation, metal deposition and adsorption. Geochemistry: Exploration, Environment, Analysis 9 (3), 203–213.

Koné, A. Y., Nasr, I. H., Traoré, B., Amiri, A., Inoubli, M. H., Sangaré, S., Qaysi, S., 2021. Geophysical contributions to gold exploration in western mali according to airborne electromagnetic data interpretations. Minerals 11 (2), 1–15.

Kovalev, K. R., Syzdykov, S. O., Kalinin, Y. A., Naumov, E. A., Baranov, V. V., Sukhorukov, V. P., Gladkov, A. S., Zhimulev, F. I., 2018. The Raigorodok stockwork gold-sulfide-quartz deposit in the North Kazakhstan gold ore province. Russian Geology and Geophysics 59 (11), 1482–1496.

Kristiansson, K., Malmqvist, L., 1987. Trace elements in the geogas and their relation to bedrock composition. Geoexploration 24 (6), 517–534.

Kuehn, S., Ogola, J., Sango, P., 1990. Regional setting and nature of gold mineralization in Tanzania and southwest Kenya. Precambrian Research 46 (1-2), 71–82.

La Flèche, M. R., Camiré, G., 1996. Geochemistry and provenance of metasedimentary rocks from the Archean Golden Pond sequence (Casa Berardi mining district, Abitibi subprovince). Canadian Journal of Earth Sciences 33 (5), 676–690.

Larin, N., Zgonnik, V., Rodina, S., Deville, E., Prinzhofer, A., Larin, V. N., 2015. Natural Molecular Hydrogen Seepage Associated with Surficial, Rounded Depressions on the European Craton in Russia. Natural Resources Research 24 (3), 369–383.

Lawrence, D. M., Lambert-Smith, J. S., Treloar, P. J., 2016. A Review of Gold Mineralization in Mali. Springer, Cham, pp. 327–351.

Lawrence, D. M., Treloar, P. J., Rankin, A. H., Boyce, A., Harbidge, P., 2013. A fluid inclusion and stable isotope study at the loulo mining district, Mali, West Africa: Implications for multifluid sources in the generation of orogenic gold deposits. Economic Geology 108 (2), 229–257.

Lefeuvre, N., Truche, L., Donzé, F. V., Ducoux, M., Barré, G., Fakoury, R. A., Calassou, S., Gaucher, E. C., 2021. Native H2 Exploration in the Western Pyrenean Foothills. Geochemistry, Geophysics, Geosystems 22 (8), e2021GC009917.

Lesage, G., Richards, J. P., Muehlenbachs, K., Spell, T. L., 2013. Geochronology, geochemistry, and fluid characterization of the late miocene buriticá gold deposit, antioquia department, Colombia. Economic Geology 108 (5), 1067–1097.

Letnikov, F. A., Narseev, A. V., 1991. Use of fluid inclusion gas surveys for the assessment of lode deposits (with reference to gold and tungsten deposits). Journal of Geochemical Exploration 42 (1), 133–142.

Lin, L. H., Hall, J., Lippmann-Pipke, J., Ward, J. A., Sherwood Lollar, B., DeFlaun, M., Rothmel, R., Moser, D., Gihring, T. M., Mislowack, B., Onstott, T. C., 2005. Radiolytic H2 in continental crust: Nuclear power for deep subsurface microbial communities. Geochemistry, Geophysics, Geosystems 6 (7).

Lintern, M. J., 2015. The association of gold with calcrete. Ore Geology Reviews 66, 132–199.

Lippmann-Pipke, J., Erzinger, J., Zimmer, M., Kujawa, C., Boettcher, M., Heerden, E. V., Bester, A., Moller, H., Stroncik, N. A., Reches, Z., 2011. Geogas transport in fractured hard rock - Correlations with mining seismicity at 3.54km depth, TauTona gold mine, South Africa. Applied Geochemistry 26 (12), 2134–2146.

Liu, C. C. ., Shi, W., Wei, J., Li, H., Feng, A., Deng, J., Yao, Y., Zhang, J., Tan, J., Liu, C. C. ., C, Shi, W, Wei, J, Li, H, Feng, A, Deng, J, Yao, Y., Y, Zhang, J, Tan, Genesis, J., 2021. Genesis of the late cretaceous longquanzhan gold deposit in the central Tan-Lu fault zone, Shandong Province, China: Constraints from noble gas and sulfur isotopes. Minerals 11 (3), 1–19.

Liu, X., Feng, X., Sun, Y., Chen, Y., Tang, Q., Zhou, X., Dong, L., Fan, S., Jiao, P., Wang, K., Wen, W., Lu, B., 2019. Acoustic and biological characteristics of seafloor depressions in the North Yellow Sea Basin of China: Active fluid seepage in shallow water seafloor. Marine Geology 414, 34–46.

Lombardo, U., Veit, H., 2014. The origin of oriented lakes: Evidence from the Bolivian Amazon. Geomorphology 204, 502–509.

Lovell, J. S., 2000. Chapter 14 Oxygen and carbon dioxide in soil air. Handbook of Exploration Geochemistry 7 (C), 451–469.

Lu, M., Ye, R., Wang, Z., Wang, X., 2019. Geogas prospecting for buried deposits under loess overburden: Taking Shenjiayao gold deposit as an example. Journal of Geochemical Exploration 197, 122–129.

Lu, Y., Guo, L., Zhang, X., Ji, C., 2012. Hydrogen production by supercritical water gasification of biomass: Explore the way to maximum hydrogen yield and high carbon gasification efficiency. International Journal of Hydrogen Energy 37 (4), 3177–3185.

Lundsten, E., Paull, C., Caress, D., Gwiazda, R., Cochrane, G., Walton, M., Nieminski, N., 2019. Commingled Seafloor Pockmarks and Micro Depressions Offshore Big Sur, California. In: AGU Fall Meeting.

Ma, G., Zhan, L., Lu, H., Hou, G., 2021. Structures in Shallow Marine Sediments Associated with Gas and Fluid Migration. Journal of Marine Science and Engineering 9 (4), 396.

Mabbutt, J. A., Fanning, P. C., 1987. Vegetation banding in arid Western Australia. Journal of Arid Environments 12 (1), 41–59.

MacKenzie, D. J., Craw, D., 2007. Contrasting hydrothermal alteration mineralogy and geochemistry in the auriferous rise & shine shear zone, Otago, New Zealand. New Zealand Journal of Geology and Geophysics 50 (2), 67–79.

MacKenzie, D. J., Craw, D., Begbie, M., 2007. Mineralogy, geochemistry, and structural controls of a disseminated gold-bearing alteration halo around the schist-hosted Bullendale orogenic gold deposit, New Zealand. Journal of Geochemical Exploration 93 (3), 160–176.

Magalhaes, N., Warr, O., Flude, S., Cutts, K., Ballentine, C., Sherwood Lollar, B., 2020. New insights on fluids from the deep hydrogeosphere of the Rio das Velhas Greenstone Belt, SE Brazil. In: American Geophysical Union, Fall Meeting 2020.

Mainson, M., Heath, C., Pejcic, B., Frery, E., 2022. Sensing Hydrogen Seeps in the Subsurface for Natural Hydrogen Exploration. Applied Sciences 12 (13), 6383.

Majeed, H., 2020. Investigation of Soil Gas Geochemistry at Thorn North Forest Ring. Ph.D. thesis, University of Toronto.

Malvoisin, B., Brunet, F., Carlut, J., Rouméjon, S., Cannat, M., 2012. Serpentinization of oceanic peridotites: 2. Kinetics and processes of San Carlos olivine hydrothermal alteration. Journal of Geophysical Research: Solid Earth 117 (B4).

Marsh, E. E., Kunk, M. J., Groves, D. I., Bierlein, F. P., Creaser, R. A., 2008. New constraints on the timing of gold formation in the Sierra Foothills province , central California. Arizona Geological Society Digest 22 (January), 369–388.

Mavrogenes, J. A., Bodnar, R. J., 1994. Hydrogen movement into and out of fluid inclusions in quartz: Experimental evidence and geologic implications. Geochimica et Cosmochimica Acta 58 (1), 141–148.

Mazzini, A., Svensen, H. H., Forsberg, C. F., Linge, H., Lauritzen, S. E., Haflidason, H., Hammer, Ø., Planke, S., Tjelta, T. I., 2017. A climatic trigger for the giant Troll pockmark field in the northern North Sea. Earth and Planetary Science Letters 464, 24–34.

McCarthy, J. H., Lambe, R. N., Dietrich, J. A., 1986. A case study of soil gases as an exploration guide in glaciated terrain - Crandon massive sulfide deposit, Wisconsin. Economic Geology 81 (2), 408–420.

McCollom, T. M., 2003. Formation of meteorite hydrocarbons from thermal decomposition of siderite (FeCO3). Geochimica et Cosmochimica Acta 67 (2), 311–317.

McCollom, T. M., 2013. Laboratory simulations of abiotic hydrocarbon formation in earth's deep subsurface. Reviews in Mineralogy and Geochemistry 75 (1), 467–494.

McCollom, T. M., Klein, F., Robbins, M., Moskowitz, B., Berquó, T. S., Jöns, N., Bach, W., Templeton, A., 2016. Temperature trends for reaction rates, hydrogen generation, and partitioning of iron during experimental serpentinization of olivine. Geochimica et Cosmochimica Acta 181, 175–200.

McCollom, T. M., Seewald, J. S., 2001. A reassessment of the potential for reduction of dissolved CO2 to hydrocarbons during serpentinization of olivine. Geochimica et Cosmochimica Acta 65 (21), 3769–3778.

McCollom, T. M., Seewald, J. S., 2003. Experimental constraints on the hydrothermal reactivity of organic acids and acid anions: I. Formic acid and formate. Geochimica et Cosmochimica Acta 67 (19), 3625–3644.

Meyer, J. J., Schutte, C. S., Galt, N., Hurter, J. W., Meyer, N. L., 2021. The fairy circles (circular barren patches) of the Namib Desert - What do we know about their cause 50 years after their first description? South African Journal of Botany 140, 226–239.

Milesi, V., Guyot, F., Brunet, F., Richard, L., Recham, N., Benedetti, M., Dairou, J., Prinzhofer, A., 2015. Formation of CO2, H2 and condensed carbon from siderite dissolution in the 200-300C range and at 50MPa. Geochimica et Cosmochimica Acta 154, 201–211.

Mohr, S., Giurco, D., Yellishetty, M., Ward, J., Mudd, G., 2015. Projection of Iron Ore Production. Natural Resources Research 24 (3), 317–327.

Mooney, H., Zavaleta, E., 2016. Ecosystems of california. University of California Press.

Moore, J. M., Picker, M. D., 1991. Heuweltjies (earth mounds) in the Clanwilliam district, Cape Province, South Africa: 4000-year-old termite nests. Oecologia 86 (3), 424–432.

Moretti, I., Brouilly, E., Loiseau, K., Prinzhofer, A., Deville, E., 2021. Hydrogen Emanations in Intracratonic Areas: New Guide Lines for Early Exploration Basin Screening. Geosciences 2021, Vol. 11, Page 145 11 (3), 145.

Mpangile, Z. M., Kazimoto, E. O., Msabi, M. M., 2020. Reconnaissance Exploration for Gold in the Misaki Area within the. Tanzania Journal of Science 46 (1), 151–170.

Mpinda, M. T., Mujinya, B. B., Mees, F., Kasangij, P. K., Van Ranst, E., 2022. Patterns and forms of copper and cobalt in Macrotermes falciger mounds of the Lubumbashi area, DR Congo. Journal of Geochemical Exploration 238, 107002.

Mueller, A. G., Groves, D. I., 1991. The classification of Western Australian greenstone-hosted gold deposits according to wallrock-alteration mineral assemblages. Ore Geology Reviews 6 (4), 291–331.

Mujinya, B. B., Adam, M., Mees, F., Bogaert, J., Vranken, I., Erens, H., Baert, G., Ngongo, M., Van Ranst, E., 2014. Spatial patterns and morphology of termite (Macrotermes falciger) mounds in the Upper Katanga, D.R. Congo. Catena 114, 97–106.

Mujinya, B. B., Mees, F., Boeckx, P., Bodé, S., Baert, G., Erens, H., Delefortrie, S., Verdoodt, A., Ngongo, M., Van Ranst, E., 2011. The origin of carbonates in termite mounds of the Lubumbashi area, D.R. Congo. Geoderma 165 (1), 95–105.

Mujinya, B. B., Mees, F., Erens, H., Dumon, M., Baert, G., Boeckx, P., Ngongo, M., Van Ranst, E., 2013. Clay composition and properties in termite mounds of the lubumbashi area, D.R. congo. Geoderma 192 (1), 304–315.

Muntean, J., Taufen, P., 2011. Geochemical exploration for gold through transported alluvial cover in Nevada: Examples from the cortez mine. Economic Geology 106 (5), 809–833.

Murray, J., Clément, A., Fritz, B., Schmittbuhl, J., Bordmann, V., Fleury, J. M., 2020. Abiotic hydrogen generation from biotite-rich granite: A case study of the Soultz-sous-Forêts geothermal site, France. Applied Geochemistry 119, 104631.

Myagkiy, A., Brunet, F., Popov, C., Krüger, R., Guimarães, H., Sousa, R. S., Charlet, L., Moretti, I., 2020a. H2 dynamics in the soil of a H2-emitting zone (São Francisco Basin, Brazil): Microbial uptake quantification and reactive transport modelling. Applied Geochemistry 112, 104474.

Myagkiy, A., Moretti, I., Brunet, F., 2020b. Space and time distribution of subsurface H 2 concentration in so-called fairy circles: Insight from a conceptual 2-D transport model. BSGF - Earth Sciences Bulletin 191 (1), 13.

Naudé, Y., van Rooyen, M. W., Rohwer, E. R., 2011. Evidence for a geochemical origin of the mysterious circles in the Pro-Namib desert. Journal of Arid Environments 75 (5), 446–456.

Neal, C., Stanger, G., 1983. Hydrogen generation from mantle source rocks in Oman. Earth and Planetary Science Letters 66 (C), 315–320.

Newell, K. D., Doveton, J. H., Merriam, D. F., Sherwood Lollar, B., Waggoner, W. M., Magnuson, L. M., 2007. H2-rich and hydrocarbon gas recovered in a deep precambrian well in Northeastern Kansas. Natural Resources Research 16 (3), 277–292.

Nivin, V. A., 2019. Occurrence forms, composition, distribution, origin and potential hazard of natural hydrogenhydrocarbon gases in ore deposits of the Khibiny and Lovozero massifs: A review. Minerals 9 (9), 535.

Niyazi, Y., Eruteya, O. E., Maitituerdi, A., Warne, M., Ierodiaconou, D., 2021. First evidence of (paleo)pockmarks in the Bass Strait, offshore SE Australia: a forced regression modulated shallow plumbing system. SSRN Electronic Journal.

Noble, R. R., Lintern, M. J., Townley, B., Anand, R. R., Gray, D. G., Reid, N., 2013. Metal migration at the North Miitel Ni sulphide deposit in the southern Yilgarn Craton: Part 3, gas and overview. Geochemistry: Exploration, Environment, Analysis 13 (2), 99–113.

Novelli, P. C., 1999. Molecular hydrogen in the troposphere: Global distribution and budget. Journal of Geophysical Research Atmospheres 104 (D23), 30427–30444.

Nwaila, G. T., Bourdeau, J. E., Jinnah, Z., Frimmel, H. E., Bybee, G. M., Zhang, S. E., Manzi, M. S., Minter, W. E., Mashaba, D., 2021. The significance of erosion channels on gold metallogeny in the Witwatersrand Basin (South Africa): Evidence from the carbon leader reef in the carletonville gold field. Economic Geology 116 (2), 265–283.

Ogungbuyi, P., Janney, P., Harris, C., 2022. Carbonatite, aillikite and olivine melilitite from Zandkopsdrift, Namaqualand, South Africa: Constraints on the origin of an unusual lamprophyre-dominated carbonatite complex and the nature of its mantle source. Lithos 418-419, 106678.

Oosthuizen, A. C., Richardson, S., 2011. Sinkholes and subsidence in South Africa. Council for Geoscience Report (number 2011-0010), 1–31.

Pandalai, H. S., Jadhav, G. N., Mathew, B., Panchapakesan, V., Raju, K. K., Patil, M. L., 2003. Dissolution channels in quartz and the role of pressure changes in gold and sulfide deposition in the Archean, greenstone-hosted, Hutti gold deposit, Karnataka, India. Mineralium Deposita 38 (5), 597–624.

Pauwels, H., Baubron, J. C., Freyssinet, P., Chesneau, M., 1999. Sorption of metallic compounds on activated carbon: Application to exploration for concealed deposits in southern Spain. Journal of Geochemical Exploration 66 (1-2), 115–133.

Pavlenkova, N. I., 1992. The Kola Superdeep Drillhole and the nature of seismic boundaries. Terra Nova 4 (1), 117–123.

Pedersen, K., 2000. Microbial processes in radioactive waste. SKB Technical Report TR-00-04. Tech. rep.

Petts, A. E., Hill, S. M., Worrall, L., 2009. Termite species variations and their importance for termitaria biogeochemistry: Towards a robust media approach for mineral exploration. Geochemistry: Exploration, Environment, Analysis 9 (3), 257–266.

Phillips, G. N., Powell, R., 2010. Formation of gold deposits: A metamorphic devolatilization model. Journal of Metamorphic Geology 28 (6), 689–718.

Plafker, G., 1964. Oriented lakes and lineaments of Northeastern Bolivia. Bulletin of the Geological Society of America 75 (6), 503–522.

Pokrovski, G. S., Kokh, M. A., Guillaume, D., Borisova, A. Y., Gisquet, P., Hazemann, J. L., Lahera, E., Del Net, W., Proux, O., Testemale, D., Haigis, V., Jonchière, R., Seitsonen, A. P., Ferlat, G., Vuilleumier, R., Saitta, A. M., Boiron, M. C., Dubessy, J., 2015. Sulfur radical species form gold deposits on Earth. Proceedings of the National Academy of Sciences of the United States of America 112 (44), 13484–13489.

Polito, P. A., Clarke, J. D., Bone, Y., Viellenave, J., 2002. A CO2-O2-light hydrocarbon-soil-gas anomaly above the Junction orogenic gold deposit: A potential alternative exploration technique. Geochemistry: Exploration, Environment, Analysis 2 (4), 333–344.

Potts, A. J., Midgley, J. J., Harris, C., 2009. Stable isotope and 14C study of biogenic calcrete in a termite mound, Western Cape, South Africa, and its palaeoenvironmental significance. Quaternary Research 72 (2), 258–264.

Preiner, M., Igarashi, K., Muchowska, K. B., Yu, M., Varma, S. J., Kleinermanns, K., Nobu, M. K., Kamagata, Y., Tüysüz, H., Moran, J., Martin, W. F., 2020. A hydrogen-dependent geochemical analogue of primordial carbon and energy metabolism. Nature Ecology and Evolution 4 (4), 534–542.

Prinzhofer, A., Moretti, I., Françolin, J., Pacheco, C., D'Agostino, A., Werly, J., Rupin, F., 2019. Natural hydrogen continuous emission from sedimentary basins: The example of a Brazilian H 2 -emitting structure. International Journal of Hydrogen Energy 44 (12), 5676–5685.

Prinzhofer, A., Tahara Cissé, C. S., Diallo, A. B., 2018. Discovery of a large accumulation of natural hydrogen in Bourakebougou (Mali). International Journal of Hydrogen Energy 43 (42), 19315–19326.

Proskurowski, G., Lilley, M. D., Seewald, J. S., Früh-Green, G. L., Olson, E. J., Lupton, J. E., Sylva, S. P., Kelley, D. S., 2008. Abiogenic hydrocarbon production at lost city hydrothermal field. Science 319 (5863), 604–607.

Rambeloson, A. R., 1999. Gold in Madagascar. Gondwana Research 2 (3), 423–431.

Ranta, E., Stockmann, G., Wagner, T., Fusswinkel, T., Sturkell, E., Tollefsen, E., Skelton, A., 2018. Fluidrock reactions in the 1.3 Ga siderite carbonatite of the GrønnedalÍka alkaline complex, Southwest Greenland. Contributions to Mineralogy and Petrology 173 (10), 1–26.

Rasmussen, B., Muhling, J. R., 2018. Making magnetite late again: Evidence for widespread magnetite growth by thermal decomposition of siderite in Hamersley banded iron formations. Precambrian Research 306, 64–93.

Ravi, S., Wang, L., Kaseke, K. F., Buynevich, I. V., Marais, E., 2017. Ecohydrological interactions within fairy circles in the Namib Desert: Revisiting the self-organization hypothesis. Journal of Geophysical Research: Biogeosciences 122 (2), 405–414.

Reid, D. L., Cooper, A. F., 1992. Oxygen and carbon isotope patterns in the Dicker Willem carbonatite complex, southern Namibia. Chemical Geology: Isotope Geoscience section 94 (4), 293–305.

Roy-Léveillée, P., Burn, C. R., 2010. Permafrost conditions near shorelines of oriented lakes in Old Crow Flats , Yukon Territory. In: 63rd Canadian Geotechnical Conference and 6th Canadian Permafrost Conference. pp. 1509–1516.

Sánchez-Palencia, F. J., Romero, D., Beltrán, A., 2018. Geo-archaeology of gold in the Pino del Oro mining area (Zamora). Melanges de la Casa de Velazquez 48 (1), 63–87.

Sarangi, S., Sarkar, A., Srinivasan, R., Patel, S. C., 2012. Carbon isotope studies of auriferous quartz carbonate veins from two orogenic gold deposits from the Neoarchean Chitradurga schist belt, Dharwar craton, India: Evidence for mantle/magmatic source of auriferous fluid. Journal of Asian Earth Sciences 52, 1–11.

Sarma, D. S., McNaughton, N. J., Fletcher, I. R., Groves, D. I., Mohan, M. R., Balaram, V., 2008. Timing of gold mineralization in the hutti gold deposit, Dharwar craton, South India. Economic Geology 103 (8), 1715–1727.

Sazonov, V. N., van Herk, A. H., De Boorder, H., 2001. Spatial and temporal distribution of gold deposits in the Urals. Economic Geology 96 (4), 685–703.

Schmandt, D., Broughton, D., Hitzman, M. W., Plink-Bjorklund, P., Edwards, D., Humphrey, J., 2013. The Kamoa copper deposit, democratic republic of Congo: Stratigraphy, diagenetic and hydrothermal alteration, and mineralization. Economic Geology 108 (6), 1301–1324.

Seewald, J. S., Zolotov, M. Y., McCollom, T., 2006. Experimental investigation of single carbon compounds under hydrothermal conditions. Geochimica et Cosmochimica Acta 70 (2), 446–460.

Sherwood Lollar, B., Frape, S. K., Fritz, P., Macko, S. A., Welhan, J. A., Blomqvist, R., Lahermo, P. W., 1993a. Evidence for bacterially generated hydrocarbon gas in Canadian shield and fennoscandian shield rocks. Geochimica et Cosmochimica Acta 57 (23-24), 5073–5085.

Sherwood Lollar, B., Frape, S. K., Weise, S. M., Fritz, P., Macko, S. A., Welhan, J. A., 1993b. Abiogenic methanogenesis in crystalline rocks. Geochimica et Cosmochimica Acta 57 (23-24), 5087–5097.

Sherwood Lollar, B., Lacrampe-Couloume, G., Slater, G. F., Ward, J., Moser, D. P., Gihring, T. M., Lin, L. H., Onstott, T. C., 2006. Unravelling abiogenic and biogenic sources of methane in the Earth's deep subsurface. Chemical Geology 226 (3-4), 328–339.

Sherwood Lollar, B., Lacrampe-Couloume, G., Voglesonger, K., Onstott, T. C., Pratt, L. M., Slater, G. F., 2008. Isotopic signatures of CH4 and higher hydrocarbon gases from Precambrian Shield sites: A model for abiogenic polymerization of hydrocarbons. Geochimica et Cosmochimica Acta 72 (19), 4778–4795.

Sherwood Lollar, B., Onstott, T. C., Lacrampe-Couloume, G., Ballentine, C. J., 2014. The contribution of the Precambrian continental lithosphere to global H2 production. Nature 516 (7531), 379–382.

Sherwood Lollar, B., Voglesonger, K., Lin, L. H., Lacrampe-Couloume, G., Telling, J., Abrajano, T. A., Onstott, T. C., Pratt, L. M., 2007. Hydrogeologic controls on episodic H2 rlease from Precambrian fractured rocks - Energy for deep subsurface life on earth and mars. Astrobiology 7 (6), 971–986.

Sillitoe, R. H., Hall, D. J., Redwood, S. D., Waddell, A. H., 2006. Pueblo Viejo high-sulfidation epithermal gold-silver deposit, Dominican Republic: A new model of formation beneath barren limestone cover. Economic Geology 101 (7), 1427–1435.

Simandl, G. J., Paradis, S., 2018. Carbonatites: related ore deposits, resources, footprint, and exploration methods. Vol. 127. Taylor & Francis.

Smee, B. W., 1984. Laboratory and Field Evidence in Support of the Electrogeochemically Enhanced Migration of Ions Through Glaciolacustrine Sediment. In: Developments in Economic Geology. Vol. 17. Elsevier, pp. 277–304.

Smith, A. J., Beukes, N. J., Gutzmer, J., 2013. The composition and depositional environments of Mesoarchean iron formations of the West Rand Group of the Witwatersrand Supergroup, South Africa. Economic Geology 108 (1), 111–134.

Snachev, A. V., Latypov, F. F., Snachev, V. I., Rassomakhin, M. A., Koshchug, D. G., Vyatkin, S. V., 2020. The Siratur Gold Deposit in Carbonaceous Rocks of an Ophiolite Association, South Urals. Moscow University Geology Bulletin 75 (6), 609–615.

Soares, M. B., Corrêa Neto, A. V., Bertolino, L. C., Alves, F. E. A., de Almeida, A. M., Montenegro da Silva, P. H., Mabub, R. O. d. A., Manduca, L. G., Araújo, I. M. C. d. P., 2018. Multistage mineralization at the hypozonal São

Sebastião gold deposit, Pitangui greenstone belt, Minas Gerais, Brazil. Ore Geology Reviews 102, 618–638.

Spiering, E. D., Pevida, L. R., Maldonado, C., González, S., Garcia, J., Varela, A., Arias, D., Martín-Izard, A., 2000. The gold belts of western Asturias and Galicia (NW Spain). Journal of Geochemical Exploration 71 (2), 89–101.

Spiridonov, A. M., Zorina, L. D., Letunov, S. P., Prokof'ev, V., 2010. The fluid regime of ore formation in the Balei gold-bearing ore-magmatic system (eastern Transbaikalia, Russia). Russian Geology and Geophysics 51 (10), 1102–1109.

Steele, A., McCubbin, F. M., Fries, M. D., Golden, D. C., Ming, D. W., Benning, L. G., 2012. Graphite in the martian meteorite Allan Hills 84001. American Mineralogist 97 (7), 1256–1259.

Stewart, A. D., Anand, R. R., 2014. Anomalies in insect nest structures at the Garden Well gold deposit: Investigation of mound-forming termites, subterranean termites and ants. Journal of Geochemical Exploration 140, 77–86.

Stewart, A. D., Anand, R. R., Balkau, J., 2012. Source of anomalous gold concentrations in termite nests, Moolart Well, Western Australia: Implications for exploration. Geochemistry: Exploration, Environment, Analysis 12 (4), 327–337.

Stromberg, J. M., Barr, E., Banerjee, N. R., 2018. Early carbonate veining and gold mineralization in the Timmins camp: Depositional context of the Dome mine ankerite veins. Ore Geology Reviews 97, 55–73.

Sukhanova, N. I., Trofimov, S. Y., Polyanskaya, L. M., Larin, N. V., Larin, V. N., 2013. Changes in the humus status and the structure of the microbial biomass in hydrogen exhalation places. Eurasian Soil Science 46 (2), 135–144.

Swain, S. K., Sarangi, S., Srinivasan, R., Sarkar, A., Bhattacharya, S., Patel, S. C., Pasayat, R. M., Sawkar, R. H., 2015. Isotope (C and O) composition of auriferous quartz carbonate veins, central lode system, Gadag Gold Field, Dharwar Craton, India: Implications to source of ore fluids. Ore Geology Reviews 70, 305–320.

Swe, Y. M., Aye, C. C., Zaw, K., 2017. Gold deposits of Myanmar. In: Geological Society Memoir. Vol. 48. Geological Society of London, pp. 557–572.

Tang, Q., Liu, X., Ji, X., Li, J., Chen, Y., Lu, B., 2021. Using seabed acoustic imagery to characterize and classify seabed sediment types in the pockmark area of the North Yellow Sea, China. Applied Acoustics 174, 107748.

Tarnita, C. E., Bonachela, J. A., Sheffer, E., Guyton, J. A., Coverdale, T. C., Long, R. A., Pringle, R. M., 2017. A theoretical foundation for multi-scale regular vegetation patterns. Nature 541 (7637), 398–401.

Tassinari, C. C. G., Pinzon, F. D., Buena Ventura, J., 2008. Age and sources of gold mineralization in the Marmato mining district, NW Colombia: A Miocene-Pliocene epizonal gold deposit. Ore Geology Reviews 33 (3-4), 505–518.

Taylor, R. D., Monecke, T., Reynolds, T. J., Monecke, J., 2021. Paragenesis of an orogenic gold deposit: New insights on mineralizing processes at the Grass Valley District, California. Economic Geology 116 (2), 323–356.

Taylor, S. R., McLennan, S. M., 1995. The geochemical evolution of the continental crust. Reviews of Geophysics 33 (2), 241–265.

Tornos, F., González Clavijo, E., Spiro, B., 1997. The filon norte orebody (Tharsis, Iberian Pyrite Belt): A proximal low-temperature shale-hosted massive sulphide in a thin-skinned tectonic belt. Mineralium Deposita 33 (1-2), 150–169.

Truche, L., Berger, G., Destrigneville, C., Guillaume, D., Giffaut, E., 2010. Kinetics of pyrite to pyrrhotite reduction by hydrogen in calcite buffered solutions between 90 and 180C: Implications for nuclear waste disposal. Geochimica et Cosmochimica Acta 74 (10), 2894–2914.

Truche, L., Bourdelle, F., Salvi, S., Lefeuvre, N., Zug, A., Lloret, E., 2021. Hydrogen generation during hydrothermal alteration of peralkaline granite. Geochimica et Cosmochimica Acta 308, 42–59.

U.S. Geological Survey, 2022. Mineral commodity summaries 2022. Tech. rep.

Van Rooyen, M. W., Theron, G. K., Van Rooyen, N., Jankowitz, W. J., Matthews, W. S., 2004. Mysterious circles in the Namib Desert: Review of hypotheses on their origin. Journal of Arid Environments 57 (4), 467–485.

Van Zuilen, M. A., Lepland, A., Teranes, J., Finarelli, J., Wahlen, M., Arrhenius, G., 2003. Graphite and carbonates in the 3.8 Ga old Isua Supracrustal Belt, southern West Greenland. In: Precambrian Research. Vol. 126. Elsevier, pp. 331–348.

Vial, D. S., DeWitt, E., Lobato, L. M., Thorman, C. H., 2007. The geology of the Morro Velho gold deposit in the Archean Rio das Velhas greenstone belt, Quadrilátero Ferrífero, Brazil. Ore Geology Reviews 32 (3-4), 511–542.

von Gunten, K., Hamilton, S. M., Zhong, C., Nesbø, C., Li, J., Muehlenbachs, K., Konhauser, K. O., Alessi, D. S., 2018. Electron donor-driven bacterial and archaeal community patterns along forest ring edges in Ontario, Canada. Environmental Microbiology Reports 10 (6), 663–672.

Wang, X., Cheng, Z., Lu, Y., Xu, L., Xie, X., 1997. Nanoscale metals in Earthgas and mobile forms of metals in overburden in wide-spaced regional exploration for giant deposits in overburden terrains. Journal of Geochemical Exploration 58 (1 SPEC. ISS.), 63–72.

Ward, J. A., Slater, G. F., Moser, D. P., Lin, L. H., Lacrampe-Couloume, G., Bonin, A. S., Davidson, M., Hall, J. A., Mislowack, B., Bellamy, R. E., Onstott, T. C., Sherwood Lollar, B., 2004. Microbial hydrocarbon gases in the Witwatersrand Basin, South Africa: Implications for the deep biosphere. Geochimica et Cosmochimica Acta 68 (15), 3239–3250.

Ward, L., 1933. Inflammable gases occluded in the Pre-Paleozoic rocks of South Australia. Trans. R. Soc. S. Aust. 57, 42–47.

Webb, A. D., Dickens, G. R., Oliver, N. H., 2006. Carbonate alteration of the Upper Mount McRae Shale at Mount Whaleback, Western Australia - Implications for iron ore genesis. In: Transactions of the Institutions of Mining and Metallurgy, Section B: Applied Earth Science. Vol. 115. Taylor & Francis, pp. 161–166.

Wei, X., Cao, J., Holub, R. F., Hopke, P. K., Zhao, S., 2013. TEM study of geogas-transported nanoparticles from the Fankou lead-zinc deposit, Guangdong Province, South China. Journal of Geochemical Exploration 128, 124–135.

Wilde, A. R., Layer, P., Mernagh, T., Foster, J., 2001. The giant muruntau gold deposit: Geologic, geochronologic, and fluid inclusion constraints on ore genesis. Economic Geology 96 (3), 633–644.

Woolley, A. R., Kjarsgaard, B. A., 2008. Carbonatite occurrences of the world: map and database. Tech. rep.

Woolnough, W., 1934. Natural Gas in Australia and New Guinea. AAPG Bulletin 18 (2), 226–242.

Yang, X. A., Li, C., Hou, K. J., rong Li, G., Liu, J. J., 2017. Magma mixing and gold mineralization in the Maevatanana gold deposit, Madagascar. Ore Geology Reviews 91, 1013–1024.

Zgonnik, V., 2020. The occurrence and geoscience of natural hydrogen: A comprehensive review. Earth-Science Reviews 203, 103140.

Zgonnik, V., Beaumont, V., Deville, E., Larin, N., Pillot, D., Farrell, K. M., 2015. Evidence for natural molecular hydrogen seepage associated with Carolina bays (surficial, ovoid depressions on the Atlantic Coastal Plain, Province of the USA). Progress in Earth and Planetary Science 2 (1), 1–15.

Zhang, C., Wang, E., Bi, Z., Han, R., Shao, J., Liu, B., Chen, J., Zeng, N., 2019. Geochronology and isotope geochemistry studies of an epithermal gold deposit in the northern Lesser Khingan Range, NE China: The Gaosongshan example. Ore Geology Reviews 105, 356–374.

Zhang, M., 2000. Chapter 4 Carbon dioxide dispersion halos around mineral deposits. Handbook of Exploration Geochemistry 7 (C), 123–132.

Zhili, H., Huaiyu, Y., Jiuhua, X., 1989. Fluid inclusion geochemistry in minerals obtained from Zhao-Ye gold metallogenetic belt, Shandong Province. Journal of Geochemical Exploration 33 (1-3), 121–133.